JOURNAL OF INFORMATION AND COMMUNICATION TECHNOLOGY
https://e-journal.uum.edu.my/index.php/jict

How to cite this article:
Ismail, N., Jumaat, A. K, Saian, R., Badarul Azam, A. S., & Mohd Ghani, N. A. S. (2026). Active contour model for vector-valued intensity inhomogeneity images corrupted by a mixture of additive gaussian and multiplicative gamma noise. *Journal of Information and Communication Technology, 25*(3), 64-97. https://doi.org/10.32890/jict2026.25.3.4

Active Contour Model for Vector-Valued Intensity Inhomogeneity Images Corrupted by a Mixture of Additive Gaussian and Multiplicative Gamma Noise

[1]Nurhuda Ismail, [2]Abdul Kadir Jumaat, [3]Rizauddin Saian, [4]Akmal Shafiq Badarul Azam & [5]Noor Ain Syazwani Mohd Ghani
[1,2&5]Faculty of Computer and Mathematical Sciences, Universiti Teknologi MARA, Shah Alam, Selangor, Malaysia
[1]Faculty of Computer and Mathematical Sciences, Universiti Teknologi MARA, Johor Branch, Pasir Gudang Campus, Johor, Malaysia
[2]Institute for Big Data Analytics and Artificial Intelligence, Universiti Teknologi MARA, Shah Alam, Selangor, Malaysia
[3]Faculty of Computer and Mathematical Sciences, Universiti Teknologi MARA, Perlis Branch, Arau Campus, Perlis, Malaysia
[4]Faculty of Computer and Mathematical Sciences, Universiti Teknologi MARA, Sarawak Branch, Mukah Campus, Sarawak, Malaysia

[1]nurhudaismail@uitm.edu.my
[*2]abdulkadir@tmsk.uitm.edu.my
[3]rizauddin@uitm.edu.my
[4]akmalshafiq@uitm.edu.my
[5]2021418828@uitm.edu.my
*Corresponding author

Received: 30/1/2026 Revised: 23/4/2026 Accepted: 5/5/2026 Published: 31/7/2026

ABSTRACT

Most of the image processing research has demonstrated the exceptional suitability of Active Contour Models (ACMs) concerning image segmentation models in image analysis as well as computer vision tasks. However, noise and intensity inhomogeneity in the vector-valued or colour images may compromise image quality and impact the results of segmentation. Most often, images are disrupted by mixed noise. To date, no existing research has addressed image segmentation under a combination of two noise types: Additive Gaussian and Multiplicative Gamma (AGMG). Thus, to fill this gap, this research proposes a variational ACM for segmenting vector-valued intensity inhomogeneity images distracted by mixed AGMG noise. Correspondingly, we developed our model by integrating dual denoising terms to reduce mixed noise and the term of optimized Laplacian of Gaussian (LoG) to recover homogeneous regions. As such, the solution to the suggested model involves minimization techniques, which are the Calculus of Variations as well as the finite difference approach. Concurrently, the models' performance, including the proposed as well as comparative models, will be assessed under low, moderate, severe, and very severe noise. As a result, the average values of the suggested framework, namely the Dice Similarity Coefficient (DSC), Jaccard Similarity Coefficient (JSC), as well as accuracy metric, were 3.29%, 1.796%, and 1.374% higher, respectively, than those of the compared models. Overall, this highlights the accuracy of our suggested model in addressing colour intensity inhomogeneity images with mixed AGMG noise for segmentation.

Keywords: Active contour model, additive Gaussian multiplicative Gamma noise, image segmentation, intensity inhomogeneity.

INTRODUCTION

Digital image processing involves transforming digital images using a computer or other digital device, conducted by a computer algorithm. The digital images may be binary, grayscale, or vector-valued (colour), and vector-valued images use Red, Green, Blue (RGB) pixels. Notably, colour is a crucial element that consists of vital information for object interpretation, including identifying the object's edges. In line with this, image processing involves numerous important tasks, among which is image segmentation, which identifies objects in images. This method involves splitting an image into subregions and is most commonly implemented in medical imaging (Anter & Abualigah, 2023), image recognition (Othman et al., 2016), and image classification (Dalavai et al., 2024).

Many image segmentation models may be classed as non-variational or variational. For example, the non-variational models include machine learning-based models. The quality of the databases determines how well the machine learning-based models are implemented (Noguerol et al., 2019). Recently, deep learning-based segmentation approaches have attracted considerable attention due to their ability to learn complex features directly from large-scale datasets (Isensee et al., 2021; Minaee et al., 2021). Recent deep learning segmentation models, such as Phi-SegNet (Ali & Hasan, 2026), the hybrid Transformer-Convolutional Neural Network (CNN) framework (Yousaf et al., 2026), and the Mamba-based decoder model (Bougourzi et al., 2026), present clear improvements in segmentation accuracy and feature learning. The Phi-SegNet model proposed by Ali and Hasan (2026) combines spatial information with frequency-domain (phase) features to better capture object boundaries and structural details, thereby achieving accurate segmentation and improving performance across different medical imaging modalities. However, this model is more complex, incurs higher computational cost, and is still in the early stages of validation. Meanwhile, the authors (Yousaf et al., 2026) introduced a hybrid Transformer-CNN framework that integrates a CNN for local feature extraction and a Transformer for global dependencies, resulting in improved segmentation and classification performance, especially for complex structures such as skin lesions. Despite this, it requires large datasets, incurs high computational cost, and is primarily designed for specific applications, limiting its general use. In addition, the Mamba-based decoder model (Bougourzi et al., 2026) focuses on improving the decoding stage through efficient sequence modelling and advanced supervision techniques, thereby enhancing segmentation quality and consistency. Still, as a newer approach, it lacks extensive validation, is complex to implement, and depends heavily on training settings. Overall, although these recent models improve segmentation performance, they still face common challenges such as high computational cost, dependence on large annotated datasets, and the lack of explicit handling of intensity inhomogeneity and noise, suggesting the need for more robust and interpretable approaches. As supported by existing studies (Litjens et al., 2017), processing datasets for deep learning models requires additional time as well as computational resources. Meanwhile, other non-variational models include region (Patil & Aggarwal, 2024) and thresholding (Wu & Yuan, 2022), which present a simple formulation and fast computation. While the models work well on simple images, they are ill-suited to processing complex images (Mazlin et al., 2023). Nevertheless, these models may provide poor segmentation results (Liu et al., 2021). Alternatively, due to their flexibility and ease of calculation, variational models are commonly employed to determine image segmentation (Liu et al., 2018). Most importantly, unlike learning-based segmentation approaches, variational models are independent of the data volume.

Variational models apply optimization principles to determine the segmentation solution. As a result, existing models can segment images accurately by maintaining the segmentation curve smooth and stable during the segmentation (Tian & Xue, 2020). In particular, the common model of variational implemented is the Active Contour Model (ACM), which consists of energy functionals (Li et al., 2008). Region-based and edge-based are groups of variational ACMs. Following this, the models suggested by Malladi et al. (1995), Caselles (1995), along with Kass et al. (1988) are edge-based implemented edge detectors to move the curve closer to the targeted edge. These pioneering models achieve accurate segmentation and produce lower computational cost by not imposing global constraints. Still, the models do not perform well at segmenting the noisy images and depend more on contour initialization (Lankton & Tannenbaum, 2008).

Noise is undesirable information that occurs in images, which affects the essential features of the images (Pathak & Sejwar, 2017). The noise in the images can be represented by two noise models, including multiplicative and additive noise. Despite this, these noise types are not always additive or multiplicative, though they can be combined (Zhao et al., 2021). As a result, in real-world applications with changing imaging conditions, a mixed noise model is most suitable for describing image noise (Wang et al., 2020). In essence, mixed noise occurs when many forms of noise are added to an image sequentially (Chithra & Santhanam, 2018). One of the popular mixed noise models is the combination of two noise types: Additive Gaussian and Multiplicative Gamma (AGMG) noise, and it frequently occurs in sectors, for instance, in medical imaging, radar imaging and remote sensing. Remarkably, mixed noise has been studied by many researchers for restoring (denoising) images, such as Chumchob et al. (2013), Li & Fan (2018) and Zhao et al. (2021). Nonetheless, to date, this type of mixed noise has not been specifically addressed within the image segmentation problem. In addition to noise in the images, intensity inhomogeneity also significantly impacts image segmentation accuracy (Mabood et al., 2022). Intensity inhomogeneity, which occurs when the intensity changes uniformly within the original homogenous region, can reduce the precision of image processing methods. Additionally, intensity inhomogeneity commonly impacts modalities of medical imaging like mammography, sonography, and Computerized Tomography (CT).

In contrast, variational region-based ACM is a model that separates pixels of background and foreground, including collecting pixels based on their intensities, thereby identifying the boundaries between regions with distinct features (Veesam & Babu, 2017). Accordingly, region-based ACMs may offer good segmentation since they are not reliant on an edge detector (Li et al., 2007). Nevertheless, the models are less dependent on contour initialization and are more capable of overseeing complicated images and topological changes compared to edge-based models. In response, this research concentrates on segmenting images using variational region-based ACMs. Subsequently, the existing models of variational region-based ACMs are introduced by several researchers (Ding et al., 2017; Ding & Weng, 2017; He et al., 2012; Li et al., 2005; Yu et al., 2020; Zhang et al., 2019; Zhang et al., 2010). He et al. (2012) introduced the Weighted Region-Scalable Fitting (WRSF) energy, which implemented a "mollifying" kernel. This produces a superior localization characteristic to mitigate the magnitude of the inhomogeneity issue. Meanwhile, the models (Ding et al., 2017; Ding & Weng, 2017) were introduced for segmenting intensity inhomogeneity images that were often encountered in medical imaging. Moreover, the authors (Yu et al., 2020) introduced a Range-Based Adaptive Bilateral Filter (RABFLR) model to reduce the noise by keeping the gradient consistency at the edge boundaries, and the model is also able to oversee intensity homogeneity in images. Building on this, the researchers (Zhang et al., 2019) can oversee noise in the images, including Gaussian as well as salt-and-pepper noise. However, the existing models are not proposed to oversee vector-valued or colour intensity inhomogeneity images corrupted by AGMG noise.

Several existing variational region-based active contour models (ACMs) have demonstrated effectiveness in segmenting vector-valued images. Studies by Chan et al. (2000), Tsai et al. (2001), Vese and Chan (2002), Badshah et al. (2018), Fang et al. (2019), and Mabood et al. (2022) have highlighted the importance of colour information in vector-valued image segmentation. By contrast, the models proposed by Chan et al. (2000), Tsai et al. (2001), and Vese and Chan (2002) are able to segment vector-valued images in the presence of noise. Similarly, the Chan-Sandberg-Vese (CSV) model by Chan et al. (2000) is computed in a vector-valued framework as a generalization of the Chan-Vese (CV) model (Chan & Vese, 2001). Meanwhile, the model of Badshah et al. (2018) effectively addresses colour-intensity inhomogeneity in images by implementing the Coefficient of Variation (CoV) formula. Remarkably, the model does not rely on a particular initial contour and requires less computational time. Still, the model may struggle to segment noisy images. The model (Fang et al., 2019) is developed from a combination of global fuzzy variational region-based ACM for segmentation, utilizing local spatial image information to address noise and intensity inhomogeneity. Although the model performs well at segmenting vector-valued images with lower processing time, it is ineffective at segmenting objects when the object's background pixels are similar. Following this, the authors (Mabood et al., 2022) can segment intensity inhomogeneity images with noise. They employed a multi-scale average filter to address inhomogeneity, using the level-set approach to achieve accurate segmentation. According to their experiments, the model is limited to overseeing Additive Gaussian (AG) noise. Nonetheless, the ACMs discussed earlier were not specifically designed and tested to segment vector-valued intensity inhomogeneity images corrupted by a mixture of AGMG noise. Thus, this research aims to formulate a new ACM to address this problem.

RELATED WORKS

Segmentation is widely employed across various sectors, for instance, in medical imaging for blood counting, in plantations for plant disease detection, and in face identification. The most challenging issue in the segmentation task is the presence of intensity inhomogeneity in images with mixed noise, specifically AGMG noise, which commonly disrupts digital images. To date, there is a lack of studies on segmenting colour intensity inhomogeneity images with AGMG noise, and this research seeks to fill this gap. Hence, Table 1 illustrates the existing related model’s benefits and weaknesses to motivate proposing the development of the GSWNC model.

According to Table 1, the model (Fang et al., 2019) is developed from a combination of global fuzzy variational region-based ACM for segmentation, utilizing local spatial image information to address noise and intensity inhomogeneity. Notably, the model performs well in segmenting intensity inhomogeneity vector-valued images disrupted by three noise types: salt and pepper, speckle, and Gaussian, with lower processing time. However, the model fails to segment objects when the background pixels are similar. Consequently, the model is more practical for segmenting vector-valued images with a particular noise.

Table 1

Overview of Existing Segmentation Models for Colour Intensity Inhomogeneity Images with Noise

Author (Year)	Segmentation Model	Strength	Limitation
Fang et al. (2019)	Fuzzy Region-based ACM with weighting, Global and Local fitting (FRAGL)	A model capable of segmenting images affected by intensity inhomogeneity with particular three noise types: salt and pepper, speckle, and Gaussian.	Segmentation is limited to single noise: Gaussian, speckle, and salt and pepper.
Ali et al. (2018)	Two-Phase (TP)	A model can segment intensity inhomogeneity images with additive, multiplicative (speckle), and a general mix of these noises.	Segmentation is limited to single noise: additive, speckle, and general mixed noise.
Azam et al. (2023)	CNN-based SegNet model with colorization techniques	Achieves strong segmentation performance by applying various colorization techniques (e.g., RGB, HSV, and pseudo-colour), enhancing feature extraction and accuracy	Performance was strongly dependent on the amount of the dataset used, and the accuracy may vary across different datasets or colorization methods.

The model introduced by Ali et al. (2018) is effective in segmenting intensity inhomogeneity images disrupted by a general mix of noise. In order to oversee noise, Ali et al. (2018) established a model by utilizing the denoising terms, which are derived from the additive noise restoration model (Rudin et al., 1992) and the multiplicative noise restoration model (Aubert & Aujol, 2008). The model (Ali et al., 2018) also incorporated local information of an image proposed by the LBF model (Li et al., 2007). It consists of a Gaussian kernel to address intensity inhomogeneity in the images. However, the Ali et al. (2018) model's segmentation results revealed few failures in segmenting adjacent objects, and their model focused on treating single and general mixed noise.

Azam et al. (2023) investigated the impact of multiple colorization methods on Magnetic Resonance Imaging (MRI) brain tumour segmentation using convolutional neural networks (CNNs), specifically the U-Net (Ronneberger et al., 2015) and SegNet (Badrinarayanan et al., 2017). MRI images are inherently grayscale, which often limits the discriminative information available for deep learning models, particularly when segmenting tumours. To address this limitation, the authors explored multiple colorization strategies, including RGB and yellow channel mappings, as well as Hue, Saturation, Value (HSV) and pseudo-colour transformations. The results revealed that colourized representations consistently improved feature extraction and segmentation accuracy. In particular, the green colour mapping diminishes the prominence of the background, allowing the meningioma tumour to stand out more clearly, and was identified as the most effective approach for achieving precise segmentation. However, these models are not specifically developed to handle images affected by intensity inhomogeneity and mixed AGMG noise, which remains a limitation.

Motivated by this, our research proposed a new variational ACM for vector-valued intensity inhomogeneity images corrupted by a mix of AGMG noise, namely the Global Segmentation with Noise for Colour (GSWNC) model. Accordingly, we incorporate the denoising term as in Ali et al. (2018) and the optimized Laplacian of Gaussian (LoG) term (Badshah et al., 2020; Ding et al., 2017) to address the primary issues, which are intensity inhomogeneity and mixed AGMG noise in the images. The subsequent section outlines the research methodology for formulating the model, while the following section presents experimental findings comparing current models with the proposed GSWNC model.

METHODOLOGY

This section details the research methodology for the proposed GSWNC model. The methodology workflow for this study is summarized and depicted in Figure 1.

Figure 1

Overview of the Suggested Framework

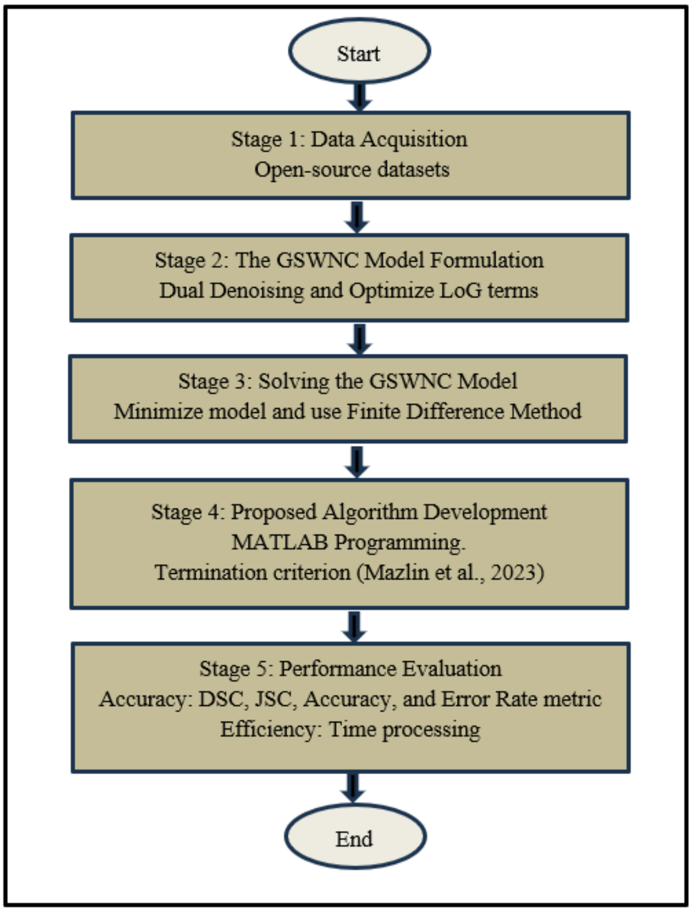

Figure 1 displays five stages of research methodology. First, image data were obtained from open-source datasets. Second, the GSWNC model is formulated. At the third stage, the GSWNC model is explained numerically. This is followed by the development of the GSWNC model's algorithm. Lastly, the segmentation outcomes are evaluated by comparing the performance of the current and newly developed models in image segmentation using numerical metrics, including accuracy and efficiency. The following subsection offers a comprehensive explanation of each stage.

Data Acquisition

This research used 20 original vector-valued images, along with their segmentation benchmarks, obtained from the authors (Chen et al., 2012; Li et al., 2018; Pandit, 2022; Wang et al., 2009; Yuzhenlu, 2022). All images were degraded by a combination of AGMG noise. In particular, the dimensions of the input images are 128 by 128 pixels and were utilized for all images.

The Mixed Noise Model

One popular mixed noise model is the AGMG noise combination. This type of mixed noise frequently occurs in various applications, including remote sensing, medical imaging, as well as radar imaging. These have been investigated by several researchers, such as Chumchob et al. (2013), Li and Fan (2018) and Zhao et al. (2021) for restoring (denoising) images. Concurrently, Zhao et al. (2021) defined the images degraded by a mixture of Gamma and Gaussian with a ratio of r. Following this, they denote $z = z(x, y)$, $z_0(x, y)$, η, and ρ as the clean image, observed image, multiplicative noise, as well as additive noise, respectively. They also consider Q the event that the noise is additive as well as its complement, $\overline{Q}$ the event that the noise is multiplicative. Meanwhile, the unknown mixture ratio for Gaussian-Gamma noise is $r = P(Q)$ where r is unknown. Thus, the mixture of AGMG noise models they define is obtained in Equation 1:

$$z_0(x, y) = \begin{cases} z(x, y) + \eta & \text{when event } Q \text{ occurs,} \\ z(x, y)\rho & \text{otherwise.} \end{cases} \tag{1}$$

Accordingly, η is an Additive Gamma (AG) noise, having a Gaussian distribution with mean 0 as well as variance σ^2. Meanwhile, the Multiplicative Gamma (MG) noise, ρ follows a Gamma distribution with shape parameter L and mean 1. The Gaussian distribution of additive noise, η at each pixel, is obtained in Equation 2, and the Gamma distribution of multiplicative noise, ρ at each pixel, is presented in Equation 3:

$$p_1(\eta) = \frac{1}{\sqrt{2\pi\sigma^2}} e^{-\frac{\eta^2}{2\sigma^2}}, \tag{2}$$

$$p_2(\rho) = \frac{L^L \rho^{L-1} e^{-L\rho}}{\Gamma(L)}, \{\rho \geq 0\}, \tag{3}$$

where the parameters σ^2 and L are unknown. Here, Γ is a gamma function parameterized by L defined by the following Equation 4:

$$\Gamma(L) = \int_0^\infty t^{L-1} e^{-t} d\,t, (L \geq 0). \tag{4}$$

Here, L is the shape parameter of the Gamma function controlling the distribution's spread, while t is a dummy variable of integration used only for mathematical definition.

Denoising Model for Additive and Multiplicative Noise

The two vital tasks in image processing are image denoising and image segmentation. Image denoising aims to reduce noise in images and preserve critical information. The denoising model is essential for the next analysis (Kollem et al., 2019). Concurrently, two classical and well-known denoising models exist: the Rudin-Osher-Fatemi (ROF) model (Rudin et al., 1992) as well as the Aubert-Aujol (AA) model (Aubert & Aujol, 2008). The ROF model treats images with additive noise. In the ROF model, a clean image is defined as $z = z(x, y)$, and the observed or noisy image is $z_0 = z_0(x, y)$ with additive noise in a bounded open subset Ω. Hence, the ROF model energy functional takes the form presented in Equation 5:

$$F_{ROF}(z(x,y)) = \int_\Omega |\nabla z| dxdy + \lambda \int_\Omega (z - z_0)^2 dxdy. \tag{5}$$

As such, $\lambda > 0$ is the parameter of the fitting term.

The AA model can address multiplicative noise. They define a clean image as $z = z(x, y)$, and the observed image or noisy image is $z_0 = z_0(x, y)$ corrupted by multiplicative noise in a bounded open subset Ω. Accordingly, the energy functional for the AA model is expressed in Equation 6:

$$F_{AA}(z(x,y)) = \int_\Omega |\nabla z| dxdy + \lambda \int_\Omega \left(\log(z) + \frac{z_0}{z} \right) dxdy. \tag{6}$$

Here, λ is the parameter of the fitting term and $\lambda > 0$. According to the two energy functionals in (5) and (6), the regularization term refers to the first term, which maintains the constructed images by smoothing them. The fitting term is the next term used to ensure that the observed and reconstructed images are closely aligned.

Global Segmentation with Noise for Colour Model Formulation

This section presents a proposed new variational global ACM for vector-valued intensity inhomogeneity images exposed to a mixture of AGMG noise. Let $z^i = z^i(x, y)$ be an observed (vector-valued) image and a clean image is $z^i = z^i(x, y)$ in a bounded domain $\Omega \subset \mathbb{R}^2$, while c_1^i and c_2^i denote the unknown intensities for the outside and inside. This corresponds to $i = 1, 2, . . , N$ channels, in which $N = 3$ represents the number of channels in the RGB colour space. Each channel corresponds to one of the three colour components: green, red, or blue. Then, the energy minimization functional of the proposed GSWNC model is formulated in Equation 7.

$$\begin{aligned}
&\min_{\phi, c_1, c_2} GSWNC(\phi, c_1, c_2) = \mu \int_\Omega \delta(\phi) |\nabla \phi| \quad d\Omega \\
&+ \lambda_1 \int_\Omega \frac{1}{N} \sum_{i=1}^{N} \left(z_0^i(x,y) - c_1^i \right)^2 H(\phi) \quad d\Omega + \lambda_2 \int_\Omega \frac{1}{N} \sum_{i=1}^{N} \left(z_0^i(x,y) - c_2^i \right)^2 (1 - H(\phi)) \quad d\Omega \\
&+ \beta_1 \int_\Omega \frac{1}{N} \sum_{i=1}^{N} (z^i(x,y) - z_0^i(x,y))^2 \quad d\Omega + \beta_2 \int_\Omega \frac{1}{N} \sum_{i=1}^{N} \left(\log z^i(x,y) + \frac{z_0^i(x,y)}{z^i(x,y)} \right) \quad d\Omega \\
&+ \alpha \frac{1}{N} \int_\Omega \sum_{i=1}^{N} L^i(x,y) H(\phi) \quad d\Omega.
\end{aligned} \tag{7}$$

The energy functional of the GSWNC model, described in Equation 7, contains six terms with fixed parameters, which are $\mu, \lambda_1, \lambda_2, \beta_1, \beta_2$ and α, while the parameter values are non-negative. The first term denotes a regularization term that controls the smoothness of the resulting segmentation contour, ϕ. It consists of the Dirac delta function, δ, and the total variation function $|\nabla\phi|$. The parameter μ controls the regularization term $\delta(\phi)|\nabla\phi|$, which enforces smoothness of the contour during evolution. A moderate value of μ is chosen to balance contour smoothness and boundary accuracy. Following this, the second and third terms represent fitting terms that govern the image data-driven force inside as well as outside the contour, where H denotes the Heaviside function. The terms are generated by the CV model (Chan &Vese, 2001). The fitting parameters, λ_1 and λ_2 regulate the data fidelity terms inside as well as outside the contour. These parameters are typically set to equal or similar values to ensure balanced segmentation between foreground and background regions across all image channels $(i = 1, 2, ..., N)$. The fourth and fifth terms are denoising terms for AG and MG noises, respectively, that are formulated by incorporating the idea of utilizing the ROF model (Rudin et al., 1992) and AA (Aubert & Aujol, 2008) fitting terms from Ali et al. (2018). The parameters β_1 and β_2 are weighting factors for the denoising terms corresponding to AGMG noise, respectively. They control the balance between the two noise components in the energy functional. In addition, we embedded the fitting image equation proposed by the Local Binary Fitting (LBF) model (Li et al., 2007) as an approximated image function z^i in the fourth and fifth terms, which contain denoising terms, as presented in Equation 8:

$$z^i(x,y) = f_1^i(x,y)H_\varepsilon(\phi) + f_2^i(x,y)(1 - H_\varepsilon(\phi)), \tag{8}$$

where $f_1^i(x,y)$ and $f_2^i(x,y)$ are computed in the following manner, as stated in Equation 9:

$$f_1^i(x,y) = \frac{\kappa_\sigma(x,y) * H_\varepsilon(\phi) z_0^i(x,y)}{\kappa_\sigma(x,y) * H_\varepsilon(\phi)}, \text{ and } f_2^i(x,y) = \frac{\kappa_\sigma(x,y) * (1 - H_\varepsilon(\phi)) z_0^i(x,y)}{\kappa_\sigma(x,y) * (1 - H_\varepsilon(\phi))}, \tag{9}$$

where K_σ is a kernel function described as a Gaussian kernel, $K_\sigma(x) = \frac{1}{(2\pi)^{n/2}\sigma^n} e^{-|x|^2 / 2\sigma^2}$ with the parameter $\sigma > 0$. The implementation of the fitting image equation from the LBF model addresses intensity inhomogeneity, and dual denoising terms from Ali et al. (2018) can treat AGMG noise in the images. The last term refers to the optimized LoG proposed by Ding et al. (2017) and Badshah et al. (2020). Accordingly, the energy functional of the optimized LoG is expressed in Equation 10:

$$E_{LoG}(L^i(x,y)) = \frac{1}{N}\int_\Omega \sum_{i=1}^{N} L^i(x,y)d\Omega = \frac{1}{N}\int_\Omega \sum_{i=1}^{N} \Big[e^{-\alpha|\nabla G_\sigma * z_0(x,y)|} \left(L^i(x,y)\right)^2 + \left(1 - e^{-\alpha|\nabla G_\sigma * z_0(x,y)|}\right) \left(L^i(x,y) - \beta\nabla^2\left(G_\sigma * z_0(x,y)\right)\right)^2 \Big] d\Omega. \tag{10}$$

$L^i(x,y)$ is the value of the optimized LoG of the image with $i = 1, 2, .., N$ channels, where $N = 3$ means a 3-channel colour format, G_σ is a Gaussian kernel function with variance, σ^2, $z_0(x,y)$ is an observed (vector-valued) image and non-negative values for the parameters α and β. Additionally, parameters such as α and σ, associated with the optimized LoG term, are chosen to control the scale of smoothing and sensitivity to image features, respectively.

Solving the Global Segmentation with Noise for Colour Model

To solve the GSWNC model obtained in Equation 7, we minimize the energy functional using a regularized version of H as well as a Dirac delta function, δ owing to $H(\phi)$ discontinuity at zero or non-differentiability at 0. Correspondingly, the regularized forms of H as well as the Dirac delta function, δ, are provided in Equation 11:

$$H_{\varepsilon}(\phi(x,y)) = \frac{1}{2}\left(1+\frac{2}{\pi}\arctan\left(\frac{\phi}{\varepsilon}\right)\right), \text{ and } \delta_{\varepsilon}(\phi(x,y)) = H_{\varepsilon}^{'}(\phi(x,y)) = \frac{\varepsilon}{\pi\left(\varepsilon^2+\phi^2\right)}. \tag{11}$$

Then, the regularized function of GWSNC is defined in Equation 12:

$$\begin{aligned}
&\min_{\phi,c_1,c_2} GSWNC_{\varepsilon}(\phi,c_1,c_2) = \mu\int_{\Omega}\delta_{\varepsilon}(\phi)\,|\nabla\phi| \quad d\Omega \\
&+\lambda_1\int_{\Omega}\frac{1}{N}\sum_{i=1}^{N}\left(z_0^i(x,y)-c_1^i\right)^2 H_{\varepsilon}(\phi) \quad d\Omega + \lambda_2\int_{\Omega}\frac{1}{N}\sum_{i=1}^{N}\left(z_0^i(x,y)-c_2^i\right)^2(1-H_{\varepsilon}(\phi)) \quad d\Omega \\
&+\beta_1\int_{\Omega}\frac{1}{N}\sum_{i=1}^{N}(z^i(x,y)-z_0^i(x,y))^2 \quad d\Omega + \beta_2\int_{\Omega}\frac{1}{N}\sum_{i=1}^{N}\left(\log z^i(x,y)+\frac{z_0^i(x,y)}{z^i(x,y)}\right) \quad d\Omega \\
&+\alpha\frac{1}{N}\int_{\Omega}\sum_{i=1}^{N}L^i(x,y)H_{\varepsilon}(\phi) \quad d\Omega.
\end{aligned} \tag{12}$$

To determine the EL equation, we minimize the problem in Equation 12 using the Calculus of Variation (Gateaux derivative) with regard to ϕ by fixing c_1^i as well as c_2^i. Hence, minimization of the variational model for the GSWNC model results in the following Equation 13:

$$\begin{aligned}
&\frac{\partial GSWNC_{\varepsilon}}{\partial\phi}(\phi,\psi) = -\mu\int_{\Omega}\psi\delta_{\varepsilon}(\phi)\nabla\cdot\left(\frac{\nabla\phi}{|\nabla\phi|}\right) \quad d\Omega + \mu\int_{\partial\Omega}\psi\cdot\left(\frac{\delta_{\varepsilon}(\phi)}{|\nabla\phi|}\right)\cdot\frac{\partial\phi}{\partial n} \quad ds \\
&+\lambda_1\int_{\Omega}\frac{1}{N}\sum_{i=1}^{N}\left(\left(z_0^i(x,y)-c_1^i\right)^2\delta_{\varepsilon}(\phi)\cdot\psi\right) \quad d\Omega \\
&-\lambda_2\int_{\Omega}\frac{1}{N}\sum_{i=1}^{N}\left(\left(z_0^i(x,y)-c_2^i\right)^2\delta_{\varepsilon}(\phi)\cdot\psi\right) \quad d\Omega \\
&+2\beta_1\int_{\Omega}\frac{1}{N}\sum_{i=1}^{N}\left[D\left(z^i(x,y)-z_0^i(x,y)\right)\delta_{\varepsilon}(\phi)\cdot\psi\right] \quad d\Omega \\
&+\beta_2\int_{\Omega}\frac{1}{N}\sum_{i=1}^{N}\left[\frac{D\left(z^i(x,y)-z_0^i(x,y)\right)\delta_{\varepsilon}(\phi)\cdot\psi}{\left(z^i(x,y)\right)^2}\right] \quad d\Omega \\
&+\alpha\int_{\Omega}\frac{1}{N}\sum_{i=1}^{N}L^i(x,y)\delta_{\varepsilon}(\phi)\cdot\psi \quad d\Omega,
\end{aligned} \tag{13}$$

with $D = f_1^i(x,y) - f_2^i(x,y)$.

Subsequently, the minimization problem obtained in Equation 13 can be solved by keeping $\phi(x,y)$ fixed, then minimizing it with respect to c_1^i and c_2^i. Then, it can be summarized in Equation 14.

$$
\begin{aligned}
c_1^i(x,y) &= \frac{\int_\Omega z_0^i(x,y) H_\varepsilon(\phi) \; d\Omega}{\int_\Omega H_\varepsilon(\phi) \; d\Omega}, && \text{(average } (z_0^i(x,y)) \text{ on } \phi \geq 0), \\
c_2^i(x,y) &= \frac{\int_\Omega z_0^i(x,y)(1 - H_\varepsilon(\phi)) \; d\Omega}{\int_\Omega (1 - H_\varepsilon(\phi)) \; d\Omega}, && \text{(average } (z_0^i(x,y)) \text{ on } \phi < 0).
\end{aligned}
\tag{14}
$$

By allowing the Neumann boundary condition $\nabla\phi \cdot n = \frac{\partial \phi}{\partial n} = 0$, we obtained the equation as in Equation 15:

$$
\begin{aligned}
&\frac{\partial GSWNC_\varepsilon}{\partial \phi}(\phi,\psi) = -\mu \int_\Omega \psi \delta_\varepsilon(\phi) \nabla \cdot \left(\frac{\nabla \phi}{|\nabla \phi|} \right) \; d\Omega + \delta_\varepsilon(\phi) \cdot \psi \\
&\left[\lambda_1 \int_\Omega \frac{1}{N} \sum_{i=1}^{N} \left(z_0^i(x,y) - c_1^i \right)^2 d\Omega - \lambda_2 \int_\Omega \frac{1}{N} \sum_{i=1}^{N} \left(z_0^i(x,y) - c_2^i \right)^2 d\Omega \right. \\
&+ 2\beta_1 \int_\Omega \frac{1}{N} \sum_{i=1}^{N} \left[D\left(z^i(x,y) - z_0^i(x,y) \right) \right] \; d\Omega \\
&\left. + \beta_2 \int_\Omega \frac{1}{N} \sum_{i=1}^{N} \left[\frac{D\left(z^i(x,y) - z_0^i(x,y) \right)}{\left(z^i(x,y) \right)^2} \right] d\Omega + \alpha \int_\Omega \frac{1}{N} \sum_{i=1}^{N} L^i(x,y) \; d\Omega \right].
\end{aligned}
\tag{15}
$$

Finally, we drive the EL equation when $GSWNC = 0$. The result is provided in Equation 16, as follows:

$$
\begin{aligned}
&\frac{\partial GSWNC_\varepsilon}{\partial \phi} \\
&= \delta_\varepsilon(\phi) \left[-\mu \nabla \cdot \left(\frac{\nabla \phi}{|\nabla \phi|} \right) + \lambda_1 \frac{1}{N} \sum_{i=1}^{N} \left(z_0^i(x,y) - c_1^i \right)^2 - \lambda_2 \frac{1}{N} \sum_{i=1}^{N} \left(z_0^i(x,y) - c_2^i \right)^2 \right. \\
&+ 2D\beta_1 \frac{1}{N} \sum_{i=1}^{N} \left(z^i(x,y) - z_0^i(x,y) \right) + D\beta_2 \frac{1}{N} \sum_{i=1}^{N} \left[\frac{\left(z^i(x,y) - z_0^i(x,y) \right)}{\left(z^i(x,y) \right)^2} \right] \\
&\left. + \alpha \frac{1}{N} \sum_{i=1}^{N} L^i(x,y) \right] = 0.
\end{aligned}
\tag{16}
$$

Next, we proceed to approximate Equation 16 by implementing an artificial time step t as well as applying the gradient descent technique illustrated in Equation 17:

$$
\frac{\partial GSWNC_\varepsilon}{\partial \phi} = -\frac{\partial \phi}{\partial t}. \tag{17}
$$

Hence, the equation of gradient descent is written in Equation 18:

$$\begin{cases} \frac{\partial \phi}{\partial t} = \delta_\varepsilon(\phi(x,y)) \left[\mu \nabla \cdot \left(\frac{\nabla \phi}{|\nabla \phi|} \right) - \lambda_1 \frac{1}{N} \sum_{i=1}^{N} \left(z_0^i(x,y) - c_1^i \right)^2 + \lambda_2 \frac{1}{N} \sum_{i=1}^{N} \left(z_0^i(x,y) - c_2^i \right)^2 \right. \\ -2D\beta_1 \frac{1}{N} \sum_{i=1}^{N} \left(z^i(x,y) - z_0^i(x,y) \right) - D\beta_2 \frac{1}{N} \sum_{i=1}^{N} \left(\frac{z^i(x,y) - z_0^i(x,y)}{\left(z^i(x,y) \right)^2} \right) \\ \left. -\alpha \frac{1}{N} \sum_{i=1}^{N} L^i(x,y) \right] = 0 \quad \text{in} \quad \Omega, \\ \delta_\varepsilon(\phi) \frac{\nabla \phi}{|\nabla \phi|} \cdot n = \frac{\delta_\varepsilon(\phi)}{|\nabla \phi|} \cdot \frac{\partial \phi}{\partial n} = 0, \\ \text{or} \\ \nabla \phi \cdot n = 0 \quad \text{or} \quad \frac{\partial \phi}{\partial n} = 0 \quad \text{on} \quad \partial \Omega. \end{cases} \tag{18}$$

Furthermore, we aim to minimize the optimized LoG term in Equation 10 by referring to t and implementing the method of gradient descent. As such, we can illustrate the solution in Equation 19, as follows:

$$\begin{aligned} \frac{\partial L}{\partial t} = -e^{-\alpha \left| \nabla G_\sigma * \frac{1}{N} \sum_{i=1}^{N} z_0^i(x,y) \right|} \frac{1}{N} \sum_{i=1}^{N} L^i(x,y) - \left(1 - e^{-\alpha \left| \nabla G_\sigma * \frac{1}{N} \sum_{i=1}^{N} z_0^i(x,y) \right|} \right) \\ \left(\frac{1}{N} \sum_{i=1}^{N} L^i(x,y) - \beta \nabla^2 \left(G_\sigma * \frac{1}{N} \sum_{i=1}^{N} z_0^i(x,y) \right) \right). \end{aligned} \tag{19}$$

Then, we address the Euler-Lagrange Partial Differential Equation (EL PDE) of the GSWNC model by discretization using the finite difference method. Therefore, the EL PDE is formulated as in Equation 20:

$$\begin{aligned} \frac{\phi_{i,j}^{n+1} - \phi_{i,j}^{n}}{\Delta t} = \delta_\varepsilon(\phi_{i,j}^{n}) \left[\mu \nabla \cdot \left(\frac{\nabla \phi_{i,j}^{n}}{|\nabla \phi_{i,j}^{n}|} \right) - \lambda_1 \frac{1}{N} \sum_{i=1}^{N} \left(z_0^i(x,y) - c_1^i \right)^2 + \lambda_2 \frac{1}{N} \sum_{i=1}^{N} \left(z_0^i(x,y) - c_2^i \right)^2 \right. \\ -2D\beta_1 \frac{1}{N} \sum_{i=1}^{N} \left(z^i(x,y) - z_0^i(x,y) \right) - D\beta_2 \frac{1}{N} \sum_{i=1}^{N} \left(\frac{z^i(x,y) - z_0^i(x,y)}{\left(z^i(x,y) \right)^2} \right) \\ \left. -\alpha \frac{1}{N} \sum_{i=1}^{N} L^i(x,y) \right]. \end{aligned} \tag{20}$$

Next, Equation 20 can be simplified further as defined in Equation 21:

$$\begin{aligned} \phi_{i,j}^{n+1} = \phi_{i,j}^{n} + \Delta t \delta_\varepsilon(\phi_{i,j}^{n}) \left[\mu \nabla \cdot \left(\frac{\nabla \phi_{i,j}^{n}}{|\nabla \phi_{i,j}^{n}|} \right) - \lambda_1 \frac{1}{N} \sum_{i=1}^{N} \left(z_0^i(x,y) - c_1^i \right)^2 + \lambda_2 \frac{1}{N} \sum_{i=1}^{N} \left(z_0^i(x,y) - c_2^i \right)^2 \right. \\ -2D\beta_1 \frac{1}{N} \sum_{i=1}^{N} \left(z^i(x,y) - z_0^i(x,y) \right) - D\beta_2 \frac{1}{N} \sum_{i=1}^{N} \left(\frac{z^i(x,y) - z_0^i(x,y)}{\left(z^i(x,y) \right)^2} \right) \\ \left. -\alpha \frac{1}{N} \sum_{i=1}^{N} L^i(x,y) \right]. \end{aligned} \tag{21}$$

Proposed Algorithm Development

Algorithm 1 outlines the steps required to implement the proposed GSWNC model. For the implementation, this research used MATLAB R2021a on an Intel Core i7-12650H CPU at 2.30 GHz with 16.0 GB of installed memory (RAM). The MATLAB programming will automatically stop when the solution achieves the tolerance value $tol = 1 \times 10^{-5}$ or the maximum number of iterations $\max it = 150$. The computational complexity of the proposed method is $O(d^2 \times N)$, in which N is the image size and d is the number of iterations, which is deduced from the work by Zhang et al. (2010). This is due to the iterative gradient descent process, in which each iteration requires pixel-wise updates across the entire image domain.

Algorithm 1. GSWNC Algorithm

1. Apply the ‘imread’ command in MATLAB to load vector-valued images.
2. Obtain vector-valued images with a mixture of AGMG noise from Equation 1.
3. Set the timestep, Δt, epsilon, ε, maximum iterations, $\max it$, tolerance, tol, parameter values of $\mu, \lambda_1, \lambda_2, \beta_1, \beta_2, \alpha$ and σ.
4. Compute the optimized LoG from Equation 19.
5. Compute as well as initialize the level set function ϕ.
6. **For** $iteration = 1$ to maximum iterations, $\max it = 150$ or $\frac{\left\| \phi_{i,j}^{n+1} - \phi_{i,j}^{n} \right\|}{\left\| \phi_{i,j}^{n} \right\|} \le tol$ **do**

   Compute the GSWNC model from Equation 21.
7. The output ϕ is described as the final solution.

In detail, the timestep Δt is selected to ensure numerical stability of the gradient descent scheme, while the tolerance tol defines the stopping criterion based on the difference between successive level set functions. Meanwhile, the maximum number of iterations, $\max it$ is fixed to limit computational cost while allowing sufficient convergence. The parameter epsilon ε is used to regularize the Dirac delta and Heavisine functions, ensuring smooth numerical approximation.

Performance Evaluation

The performance evaluation is conducted using assessment tools to assess accuracy and efficiency. The accuracy assessment tools comprise the Dice Similarity Coefficient (DSC), the Jaccard Similarity Coefficient (JSC), the accuracy metric, and the Error Rate metric. Meanwhile, the efficiency assessment tool is processing time. This research applies a confusion matrix to assess the performance of segmentation models. The matrix provides an analysis of True Negative (TN), True Positive (TP), False Positive (FP), and False Negative (FN) predictions. Thus, all analyses are elaborated on. The confusion matrix enhances the understanding of the JSC, DSC, accuracy metric, and error metric (Ataş, 2023). DSC and JSC are widely used in image segmentation. These coefficients measure the similarity between the performance models. The DSC is likewise referred to as the F1 score. The equation can be written as in Equation 22:

$$DSC = \frac{2 \times TP}{(2 \times TP + FP + FN)} \tag{22}$$

This research will also assess the models' performance employing the JSC or Jaccard Index, namely Intersection over Union (IOU), as given in Equation 23:

$$JSC = \frac{DSC}{2-DSC} \tag{23}$$

The accuracy metric is determined by the closeness of the segmentation result (Hossin & Sulaiman, 2015) and is outlined as stated in Equation 24:

$$Accuracy = \frac{(TP+TN)}{(FN+FP+TP+TN)} \tag{24}$$

The error metric is a complementary accuracy statistic that assesses the generated solution by the proportion of inaccurate predictions. The Error Rate metric, or misclassification error, is the ratio of inaccurate predictions to the number of examples assessed (Hossin & Sulaiman, 2015). The advantages of this metric are easy to evaluate, and the formula is represented in Equation 25:

$$Error = \frac{(FP+FN)}{(TP+TN+FN+FP)} \tag{25}$$

To conclude, for accuracy testing such as DSC, JSC, and the accuracy metric, a value approaching 1 indicates that the model achieves accurate segmentation. Conversely, the smaller error value approaching 0 indicates better segmentation in the Error Rate metric. The range value for each accuracy test is from 0 to 1.

EVALUATION AND RESULTS

This section illustrates the proposed GSWNC model's advantages for segmenting vector-valued intensity inhomogeneity images contaminated by mixed AGMG noise compared with existing models. The proposed GSWNC model (M3) will be compared with the existing models M1 (Fang et al., 2019) and M2 (Ali et al., 2018). According to our numerical evaluation, we set the following parameters: the timestep, Δt, epsilon, ε, maximum iterations, $\max it$, tolerance, tol, and parameter values of $\mu, \lambda_1, \lambda_2, \beta_1, \beta_2, \alpha$ and σ are fixed values. The values are specified as follows: $\Delta t = 0.0001$, $\varepsilon = 1$, $tol = 0.00001$, $\max it = 150$, $\lambda_1 = 0.6$, $\lambda_2 = 1$, $\beta_1 = 0.1$, $\beta_2 = 0.9$, $\alpha = 1$, and $\sigma = 10$. Meanwhile, the μ parameter varies across experiments. A larger μ value is assigned when the target object is large, and the object cannot be detected due to the presence of noise. In contrast, for detecting smaller objects, μ should be set to a smaller value. The specific value μ used in each case will be provided along with the corresponding initial level set function. Figure 2 below displays all 20 vector-valued intensity inhomogeneity input images with square initial contours in green, corrupted by a mixture of AGMG noise under the different true noise parameters, σ^2 and L, which represent different noise intensity levels. In detail, the AG noise follows a Gaussian distribution with a mean of 0 as well as a different variance σ^2. Meanwhile, the MG noise is distributed according to the Gamma distribution with mean 1 as well as varying shape parameters L. The intensity inhomogeneity input images were corrupted by a mixture of AGMG noise under the different true noise parameters, variance, σ^2, for Gaussian noise, as well as the shape parameter, L, for Gamma noise. The 20 original images were corrupted with a combination of AGMG noise with a fixed mixture ratio of Gaussian-Gamma $r = 0.5$ under the following combination of true parameters: $\sigma^2 = 0.0001, L = 1000$, $\sigma^2 = 0.0009, L = 500$, $\sigma^2 = 0.001, L = 100$ and $\sigma^2 = 0.01, L = 50$. The larger σ^2 indicates severe Gaussian noise, while a lower L indicates severe Gamma noise (Li & Fan, 2018). Consequently, each original image generated four noise intensity levels, namely low, moderate, severe and very severe noise, respectively. For comparative evaluation, these noise levels were designated as Experiment 1 (Exp 1), Experiment 2 (Exp 2), Experiment 3 (Exp 3), and Experiment 4 (Exp 4), respectively. Consequently, a total of 80 noisy input images were applied in the experiments.

Figure 2

Intensity Inhomogeneity Input Images with Initial Contours Corrupted by a Mixture of AGMG Noise with Different Noise Intensity Levels

Exp 1	Exp 2	Exp 3	Exp 4
$\sigma^2 = 0.0001$, $L = 1000$	$\sigma^2 = 0.0009$, $L = 500$	$\sigma^2 = 0.001$, $L = 100$	$\sigma^2 = 0.01$, $L = 50$

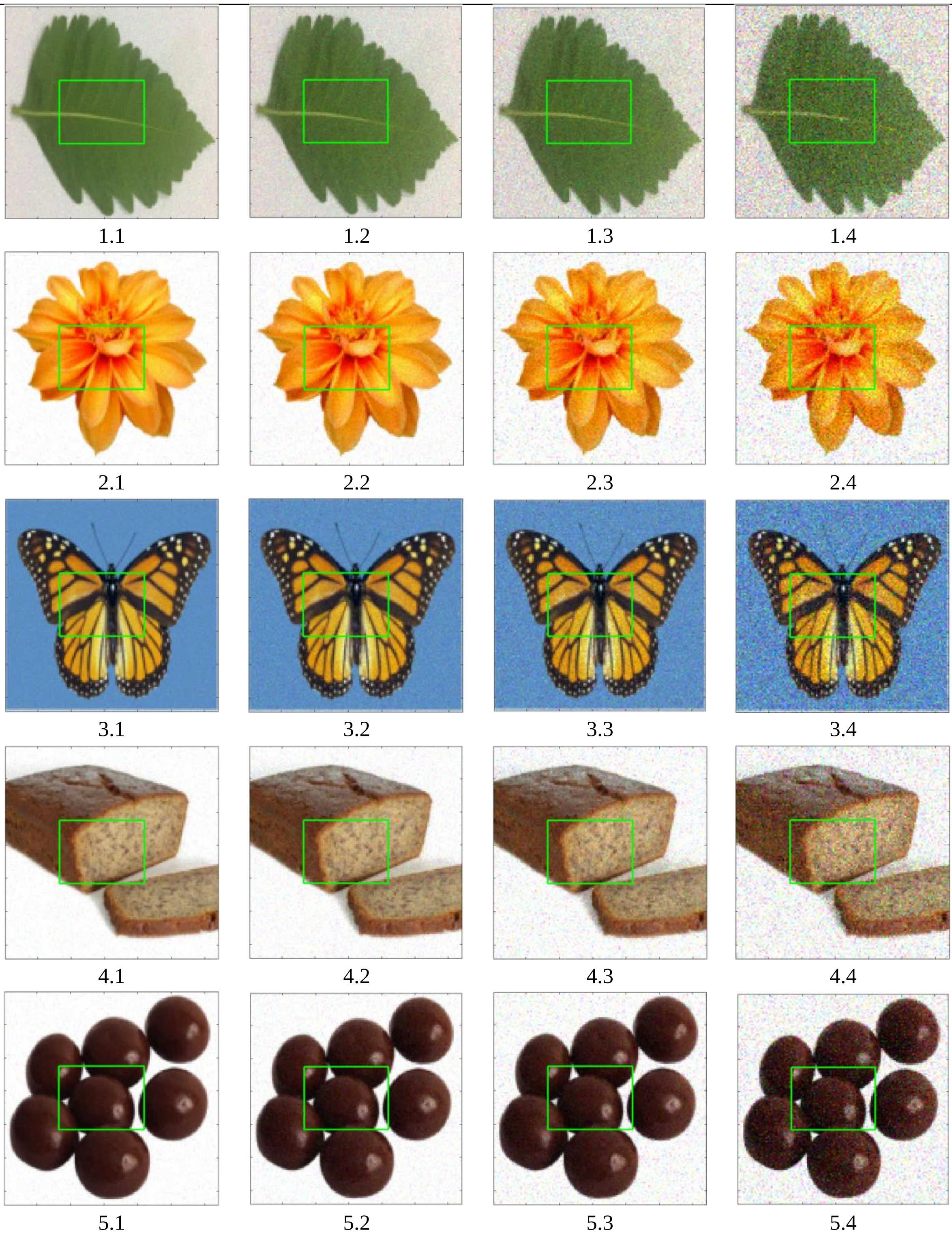

(continued)

Exp 1 $\sigma^2 = 0.0001$, $L = 1000$	Exp 2 $\sigma^2 = 0.0009$, $L = 500$	Exp 3 $\sigma^2 = 0.001$, $L = 100$	Exp 4 $\sigma^2 = 0.01$, $L = 50$
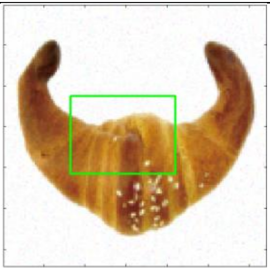	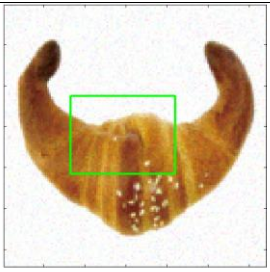	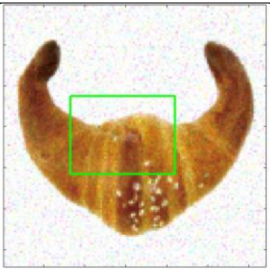	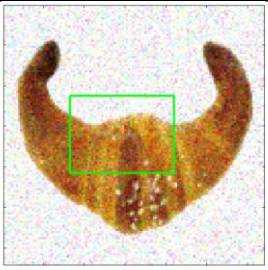
6.1	6.2	6.3	6.4
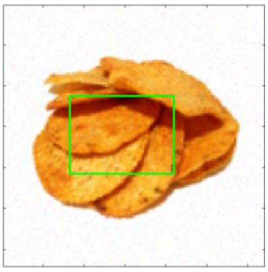	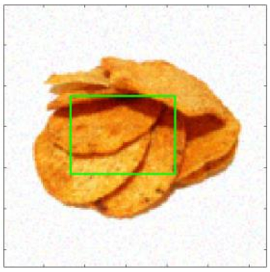	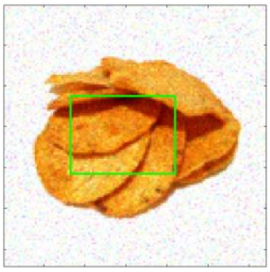	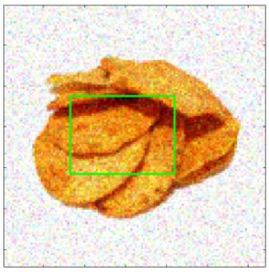
7.1	7.2	7.3	7.4
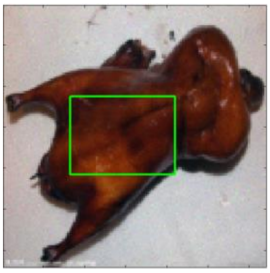	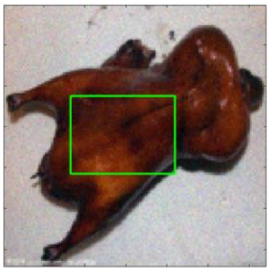	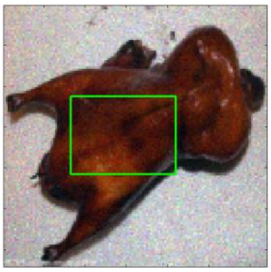	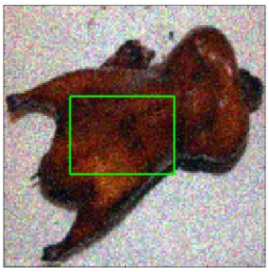
8.1	8.2	8.3	8.4
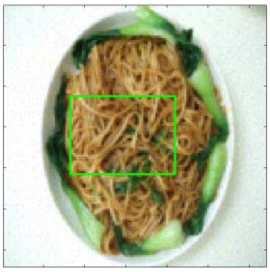	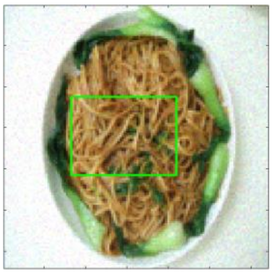	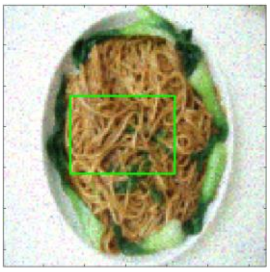	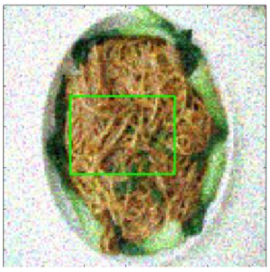
9.1	9.2	9.3	9.4
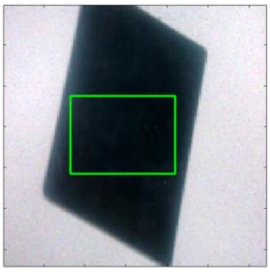	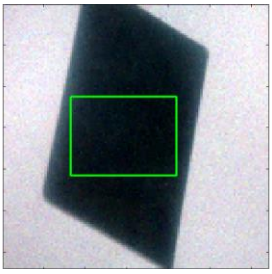	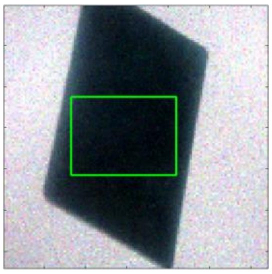	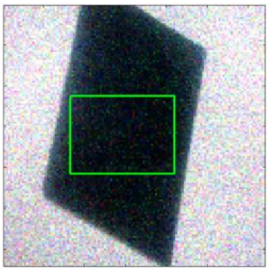
10.1	10.2	10.3	10.4

(continued)

Exp 1 $\sigma^2=0.0001$, $L=1000$	Exp 2 $\sigma^2=0.0009$, $L=500$	Exp 3 $\sigma^2=0.001$, $L=100$	Exp 4 $\sigma^2=0.01$, $L=50$
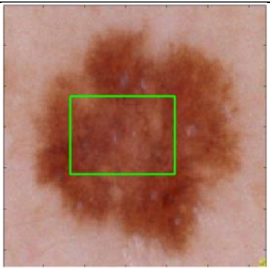 11.1	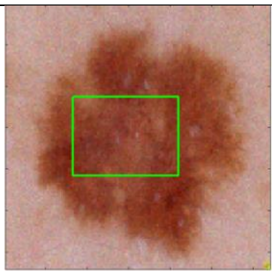 11.2	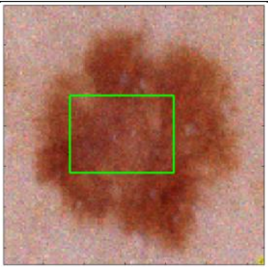 11.3	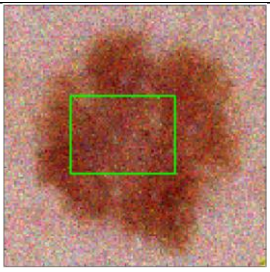 11.4
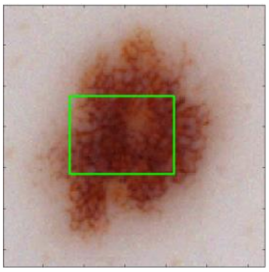 12.1	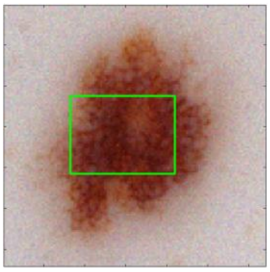 12.2	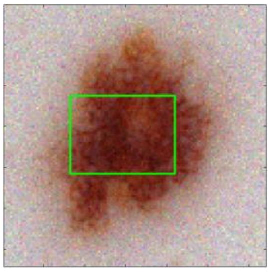 12.3	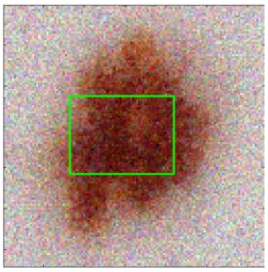 12.4
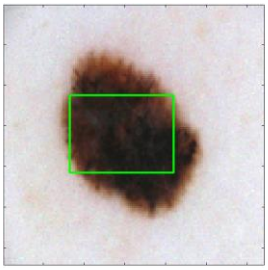 13.1	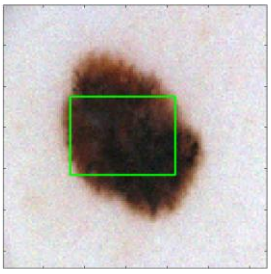 13.2	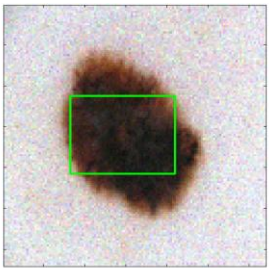 13.3	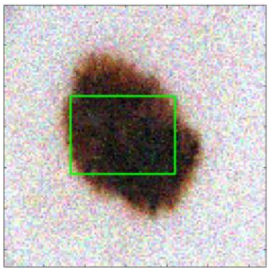 13.4
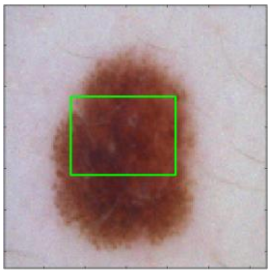 14.1	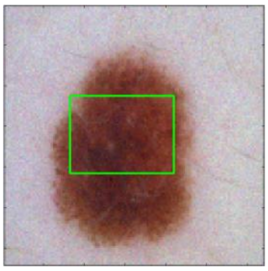 14.2	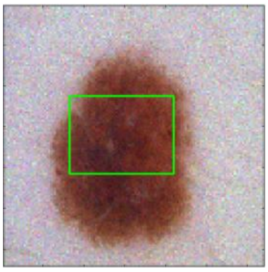 14.3	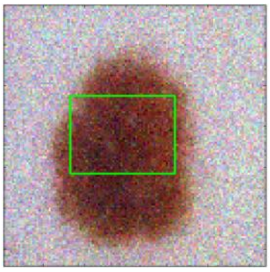 14.4
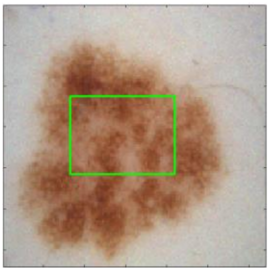 15.1	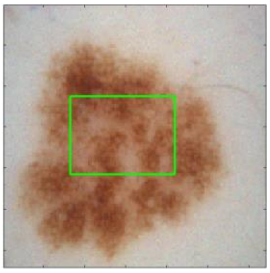 15.2	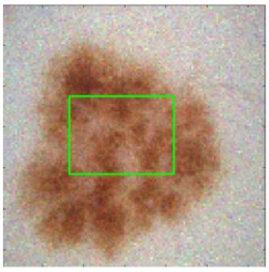 15.3	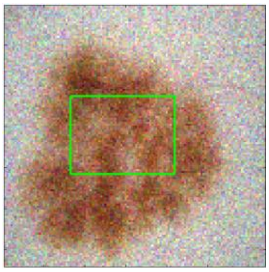 15.4

(continued)

Exp 1 $\sigma^2=0.0001$, $L=1000$	Exp 2 $\sigma^2=0.0009$, $L=500$	Exp 3 $\sigma^2=0.001$, $L=100$	Exp 4 $\sigma^2=0.01$, $L=50$
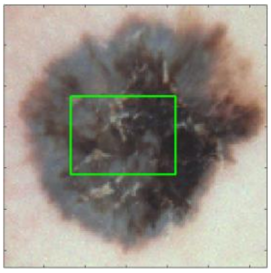 16.1	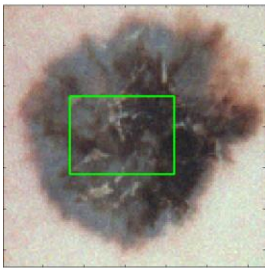 16.2	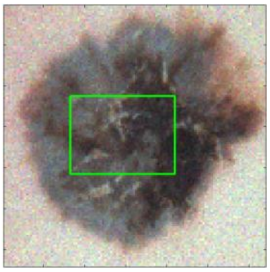 16.3	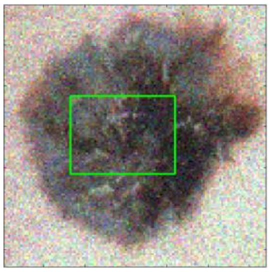 16.4
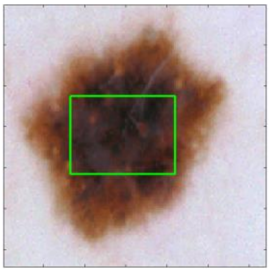 17.1	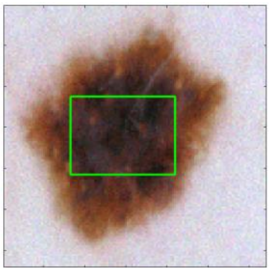 17.2	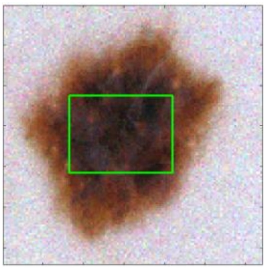 17.3	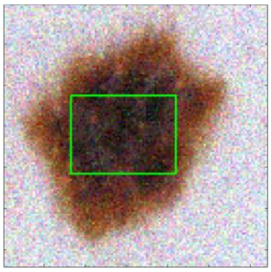 17.4
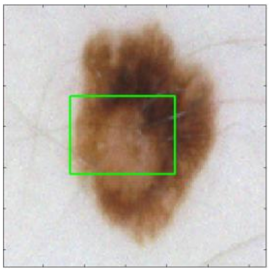 18.1	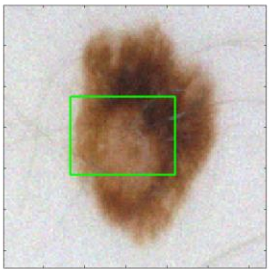 18.2	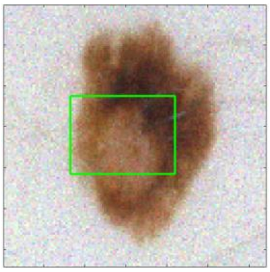 18.3	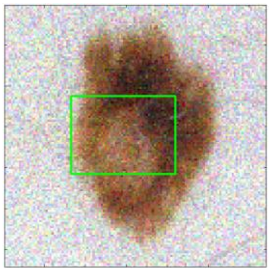 18.4
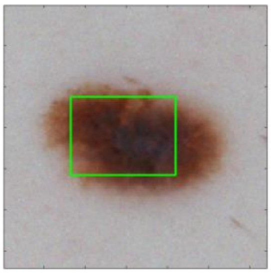 19.1	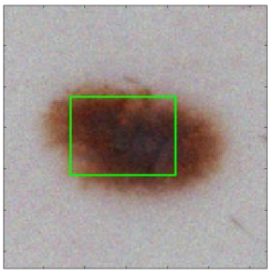 19.2	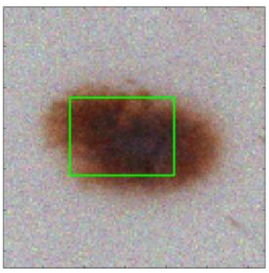 19.3	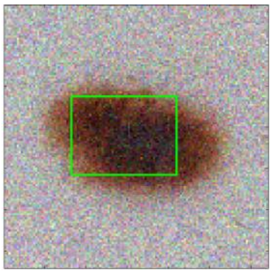 19.4
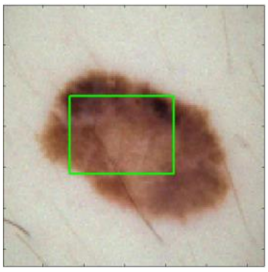 20.1	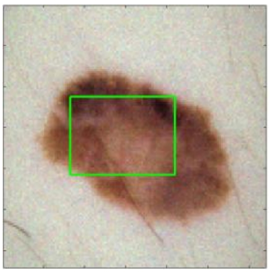 20.2	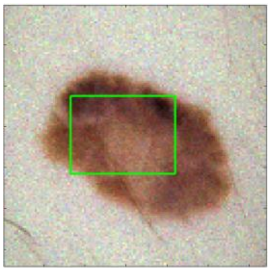 20.3	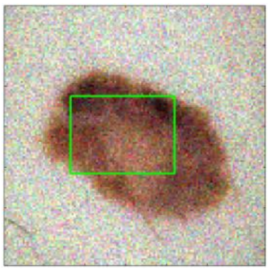 20.4

From Figure 2, this study used input images comprising 80 vector-valued intensity inhomogeneity images corrupted by AGMG noise, with initial segmentation contours represented in square green. Images 1.1 to 10.4 are natural images. Meanwhile, the remaining images (11.1-20.4) are skin cancer images. Then, the segmentation results for all input images corrupted by four different noise intensity levels are compared between the proposed M3 model and the comparison models M1 and M2. Therefore, Figure 3 depicts Exp 1, Exp 2, Exp 3, as well as Exp 4 as the result of segmentation for the four sample input images (out of 80 input images) under varying noise intensity levels of a mixture of AGMG.

Figure 3

Segmentation Result for Four Sample Segmented Images under Different Noise Intensity Levels of a Mixed AGMG Noise for All Models

Exp/ Model	M1	M2	M3
Exp 1 σ^2=0.0001, L=1000			

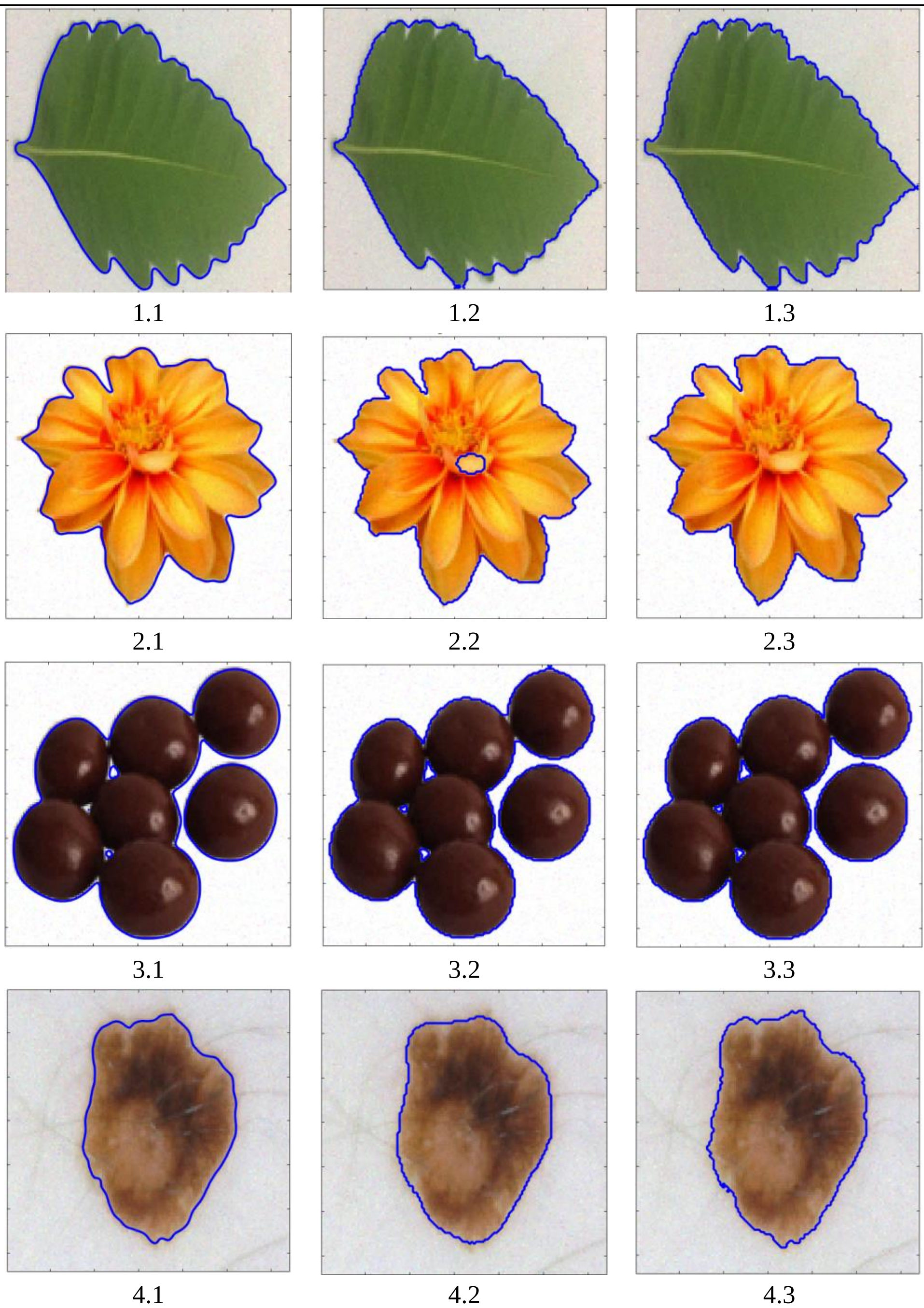

(continued)

Exp/ Model	M1	M2	M3
	 5.1	 5.2	 5.3
	 6.1	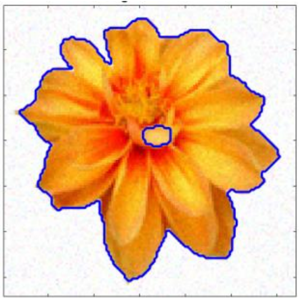 6.2	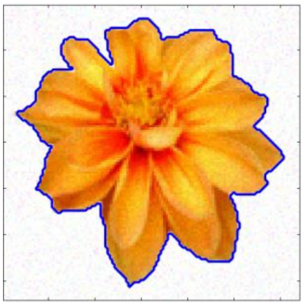 6.3
Exp 2 $\sigma^2=0.0009$, $L=500$	 7.1	 7.2	 7.3
	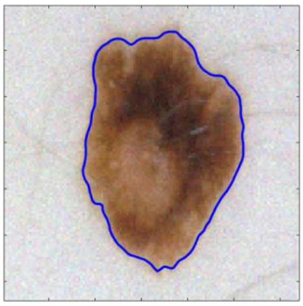 8.1	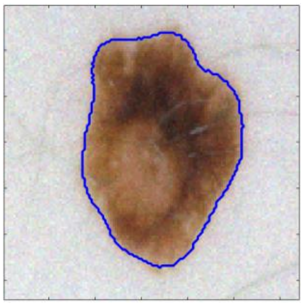 8.2	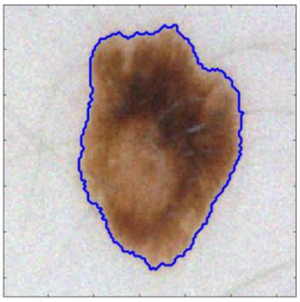 8.3

(continued)

Exp/ Model	M1	M2	M3
Exp 3 $\sigma^2=0.001$, $L=100$	 9.1	 9.2	 9.3
	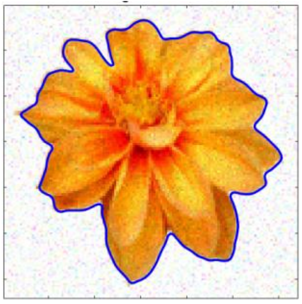 10.1	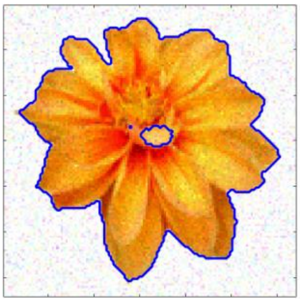 10.2	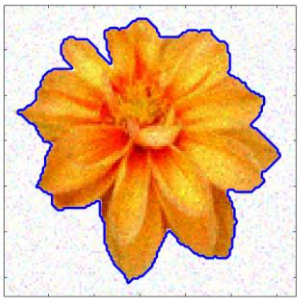 10.3
	 11.1	 11.2	 11.3
	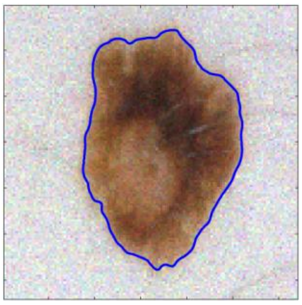 12.1	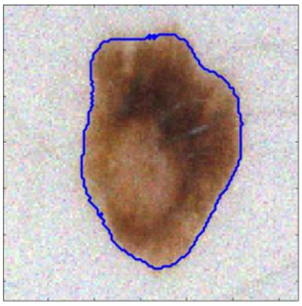 12.2	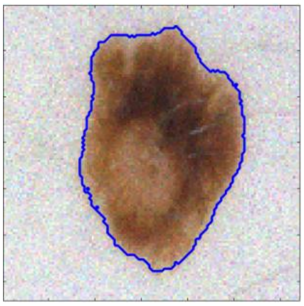 12.3

(continued)

Exp/ Model	M1	M2	M3
	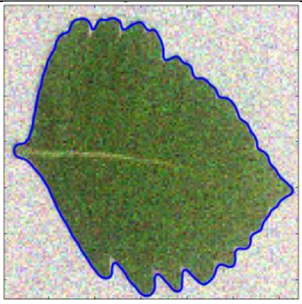	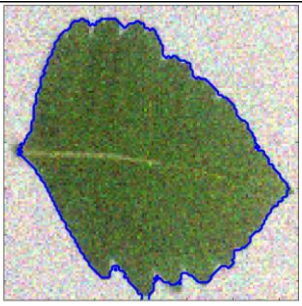	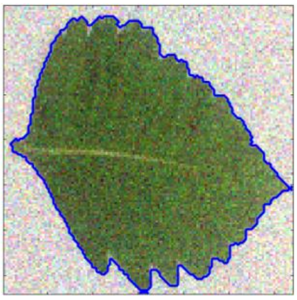
	13.1	13.2	13.3
	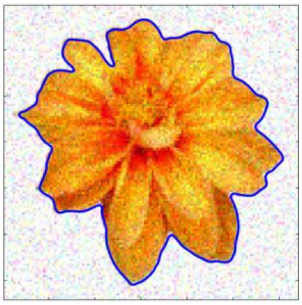	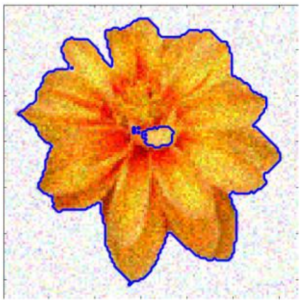	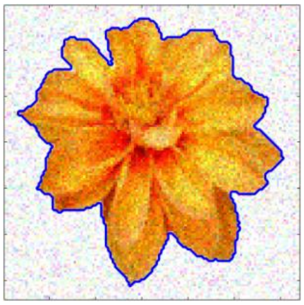
Exp 4 $\sigma^2=0.01$, $L=50$	14.1	14.2	14.3
			
	15.1	15.2	15.3
	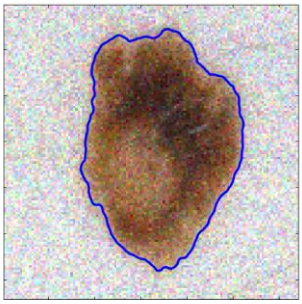	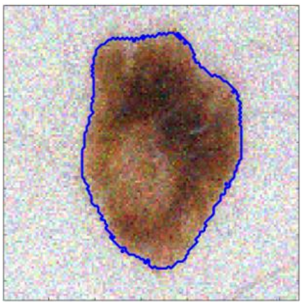	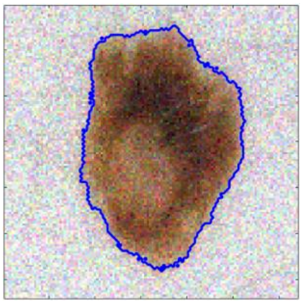
	16.1	16.2	16.3

Based on Figure 3, images 1.1 to 1.3, 2.1 to 2.3, 3.1 to 3.3, and 4.1 to 4.3 illustrate the segmentation results for M1 to M3 obtained in Exp 1, where a low AGMG mixture tests the images. As a result, for M2, we obtained image 2.2, which displays over-segmentation within the segmented object. The other images demonstrate good segmentation for M1-M3. Meanwhile, images 5.1 to 5.3, 6.1 to 6.3, 7.1 to 7.3, and 8.1 to 8.3 show the segmentation results for M1 to M3 from Exp 2. This second test, with a moderate mixture of AGMG noise, suggests that M2, illustrated in image 6.2, exhibits over-segmentation within the segmented object. It is also observed that the images in Exp 2 present accurate segmentation. Following this, the third test, denoted Exp 3, uses a severe AGMG noise mixture. The segmentation results, as portrayed in images 9.1 to 9.3, 10.1 to 10.3, 11.1 to 11.3, and 12.1 to 12.3, contribute to an analysis of M2, which suggests that over-segmentation is present within the interior of the segmented region, as indicated in image 10.2. The remaining images obtained in the third experiment are well-segmented. Lastly, the result for Exp 4 uses a very severe mixture of AGMG noise presented in 13.1 to 13.3, 14.1 to 14.3, 15.1 to 15.3, and 16.1 to 16.3. As a result, M2, as displayed in image 14.2, indicates the segmented object exhibits internal over-segmentation. The remaining segmentation results for this experiment demonstrate good segmentation.

In addition to qualitative visual observations, the experiment will be evaluated using quantitative accuracy measures (JSC, DSC, accuracy metric, and error metric) and quantitative efficiency metrics (processing time). Values of JSC, DSC, and the accuracy metric approaching 1 indicate that the model is achieving accurate segmentation. Conversely, a smaller error metric value, approaching 0, indicates better segmentation. The range value for each accuracy test is from 0 to 1. Accordingly, Table 2 presents the average quantitative results for segmenting all input images at distinct intensity levels of the AGMG mixture noise.

Table 2 presents average accuracy and efficiency values for global segmentation of all input images at different noise intensity levels using a mixture of AGMG noise. A bar chart showing the average value for each quantitative result is constructed, as illustrated in Figure 4, to provide a comprehensive overview of the results.

Table 2

The Average Quantitative Result for All Input Images for All Models

Exp/ Model	M1	M2	M3
	Jaccard/Dice/Accuracy/Error/Processing Time (seconds)		
Exp 1 σ^2=0.0001, L=1000	0.8601/0.9181/ 0.9325/0.1108/ 1.7257	0.8691/0.9283/ 0.9358/0.0642/ 55.3961	0.8898/0.9404/ 0.9451/0.0549/ 24.3718
Exp 2 σ^2=0.0009, L=500	0.8611/0.9237/ 0.9333/0.0667/ 2.5751	0.8691/0.9283/ 0.9357/0.0643/ 58.6629	0.8900/0.9405/ 0.9451/0.0549/ 26.1856
Exp 3 σ^2=0.001, L=100	0.8626/0.9247/ 0.9339/0.0661/ 3.0376	0.8699/0.9287/ 0.9359/0.0641/ 52.6452	0.8909/0.9410/ 0.9456/0.0544/ 24.2263
Exp 4 σ^2=0.01, L=50	0.8673/0.9275/ 0.9351/0.0649/ 3.5611	0.8672/0.9270/ 0.9348/0.0653/ 52.8038	0.8958/0.9439/ 0.9478/0.0522/ 24.0204

Based on Table 2, Figure 4(a), and Figure 4(b), image segmentation with a very severe mixture of AGMG noise, assessed in Exp 4, indicates that the proposed GSWNC model (M3) achieves the highest DSC and JSC values for image segmentation compared to other experiments and existing models. The results yielded an average JSC value of M3 of 0.8958, which is 3.286% and 3.298% higher than M1 and M2, respectively. Obviously, the average DSC value is obtained from the same experiment; M3 recorded 0.9439, which is 1.768% and 1.823% higher than M1 and M2, respectively.

Furthermore, Table 2, Figure 4(c), and Figure 4(d) illustrate that M3 leads with an average accuracy of 0.9478 for segmenting images corrupted by very severe mixed AGMG noise, and its average error naturally becomes the lowest. Hence, M3 is a practical model to segment colour intensity inhomogeneity images disrupted by mixed AGMG noise. It is due to the implementation of dual denoising terms integrated with local image information to treat intensity inhomogeneity in images with mixed AGMG noise. In addition, the segmentation is made more accurate by incorporating an optimized

LoG term into the GSWNC energy functional to ensure homogeneous regions are smooth and to recover the boundary object. Consequently, there are several potential reasons for less accurate segmentation of M1 and M2 in segmenting vector-valued intensity inhomogeneity images with a mix of AGMG noise. For M1, the model was designed to oversee a single noise (Fang et al., 2019). Meanwhile, according to Ali et al. (2018), for M2, the model can segment images interrupted by general mixed noise. Still, it might not be able to segment images corrupted with a specific mixture of AGMG noise.

According to Table 2 and Figure 4(e), the efficiency assessment based on processing time for the M1, M2, and M3 models showed that the M2 model had the longest average processing time when segmenting intensity inhomogeneity images interrupted by a moderate mixture of AGMG noise. This is represented in Exp 2, with a processing time of 58.6629 seconds, followed by M3 at 26.1856 seconds, and M1 at 2.5751 seconds. Notably, the most likely cause of M2 having the highest computational cost, followed by M3, is that both models incorporated their energy functional with a dual denoising term, which consists of fitting an image equation. In essence, this dual denoising term uses a Gaussian kernel and a convolution operation, which can significantly increase computational cost and make these models the slowest to segment images.

Figure 4

Average Values of (a) JSC, (b) DSC, (c) Accuracy Metric, (d) Error Rate Metric, and (e) Processing Time According to Different Noise Intensity Levels for All Models

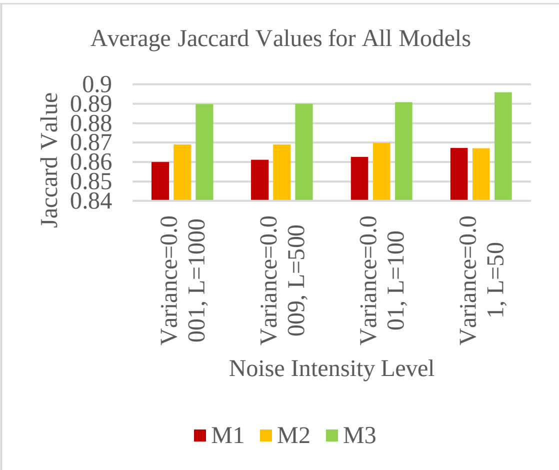

(a)

(b)

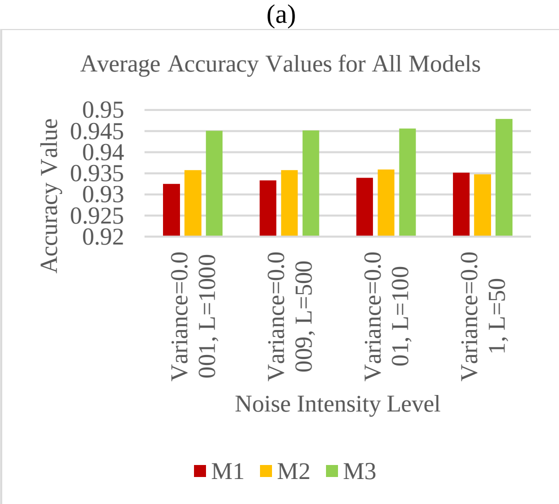

(c)

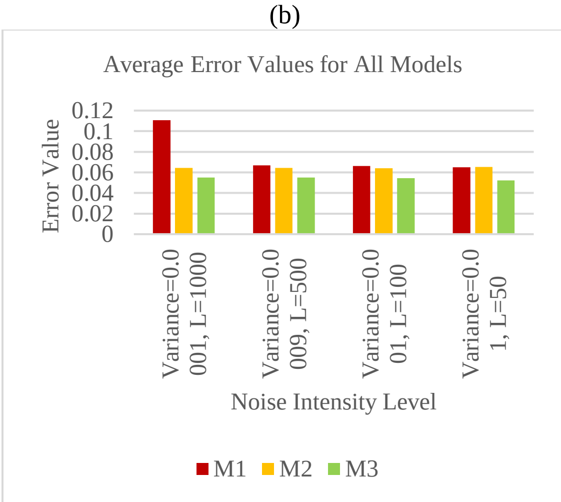

(d)

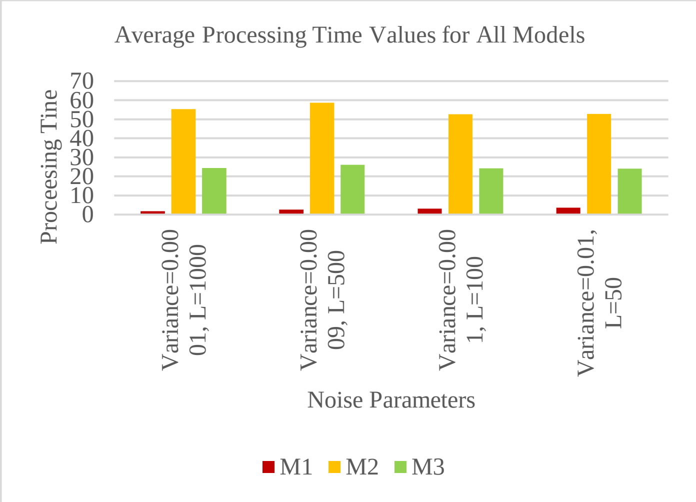

(e)

In addition to the qualitative and quantitative evaluation, a deeper analytical evaluation of the suggested GSWNC model highlights several important advantages and limitations. The model's improved performance is primarily attributed to the incorporation of dual denoising terms and a refined LoG term. Here, the dual denoising terms enable the model to effectively handle the coexistence of AGMG noise, which commonly occurs in practical imaging environments. Simultaneously, the optimized LoG term enhances boundary detection and promotes homogeneous region reconstruction, thereby reducing over-segmentation and improving segmentation accuracy. Compared to existing models, M1 is limited to handling a single type of noise, which limits its robustness in mixed-noise settings. Meanwhile, although M2 considers mixed noise, it is not specifically designed for AGMG noise, which explains the observed inconsistencies, such as over-segmentation in several experiments. In contrast, the proposed model explicitly addresses AGMG noise, resulting in more stable and accurate segmentation across different noise intensity levels.

However, the proposed model is not without limitations. First, the inclusion of dual denoising terms increases computational complexity, leading to higher processing time compared to simpler models such as M1. Second, the model's performance is contingent upon the selection of parameter values, which may require careful tuning for optimal results. Third, the current study is limited to Two-Dimensional (2D) vector-valued images, and the model has not yet been extended to more complex data, such as Three-Dimensional (3D) medical images or large-scale datasets. Despite these limitations, the robustness of the proposed GSWNC model under severe mixed noise conditions demonstrates its strong prospective value for practical uses, particularly in medical imaging, remote sensing, as well as other domains in which image quality is significantly degraded by complex noise.

Comparison between Global Segmentation with Noise for Colour Model with Convolutional Neural Networks

The GSWNC model (M3) is further compared with the model (M4) introduced by Azam et al. (2023), that includes effects of several colorization methods on input data utilizing CNNs, particularly the SegNet model. Both models (M3 and M4) aim to address intensity inhomogeneity and noise in vector-valued images for image segmentation. Four experiments were conducted for both comparison models using 80 noisy input images (Figure 2). Figure 5 depicts Exp 1, Exp 2, Exp 3, and Exp 4, shown as segmentation results for three sample input images (out of 80 input images) under varying noise intensities for a mixture of AGMG.

We present images 1.1-1.2, 2.1-2.2, and 3.1-3.2 as the segmentation results for M3 and M4 from Exp 1, which tested low noise. As a result, images 1.2 and 2.2 exhibit under-segmentation within the segmented object, while M3 presents good segmentation. Meanwhile, images 4.1 to 4.2, 5.1 to 5.2, and 6.1 to 6.2 were the segmentation results for Exp 2, which involved moderate image noise and was conducted by M3 and M4. Hence, M4 produced under-segmentation at the object boundaries, as displayed in images 4.2 and 5.2, whereas M3 produced smooth segmentation within object boundaries. The other result, depicted in Figure 5, is obtained from Exp 3 and Exp 4, which were tested under severe and very severe noise, respectively, as displayed in images 7.1 to 7.2, 8.1 to 8.2, 9.1 to 9.2, 10.1 to 10.2, 11.1 to 11.2 and 12.1 to 12.2. As a result, images 7.2, 8.2, 10.2 and 11.2 indicated that M4 was producing under-segmentation in the object regions, while images 9.2 and 12.2 illustrate over-segmentation beyond the object boundaries. Conversely, M3 illustrates accurate segmentation. Overall, the visual outcomes reveal that the developed GSWNC model (M3) provides more accurate image segmentation for crucial intensity inhomogeneity and mixed AGMG noise.

Figure 5

Segmentation Result for Three Sample Segmented Images under Different Noise Intensity Levels of a Mixed AGMG Noise for All Models

Exp/ Model	M3	M4
		
	1.1	1.2
Exp 1 $\sigma^2 = 0.0001,$ $L = 1000$		
	2.1	2.2
	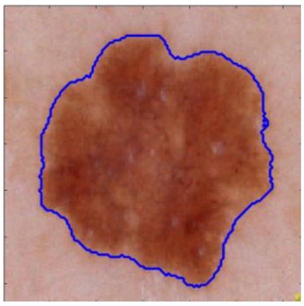	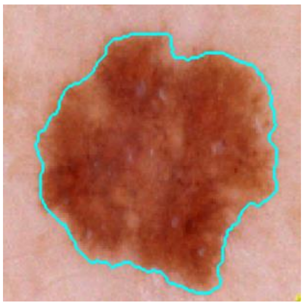
	3.1	3.2

(continued)

Exp/ Model	M3	M4
	 4.1	 4.2
Exp 2 $\sigma^2=0.0009$, $L=500$	 5.1	 5.2
	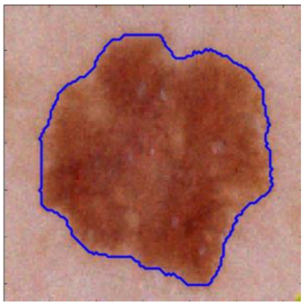 6.1	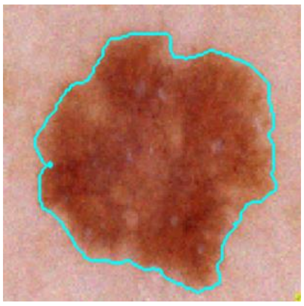 6.2
	 7.1	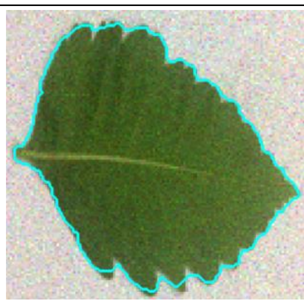 7.2
Exp 3 $\sigma^2=0.001$, $L=100$	 8.1	 8.2

(continued)

Exp/ Model	M3	M4
	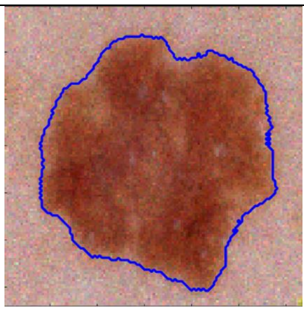 9.1	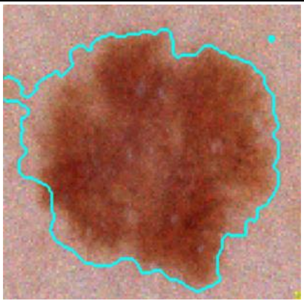 9.2
Exp 4 $\sigma^2 = 0.01$, $L = 50$	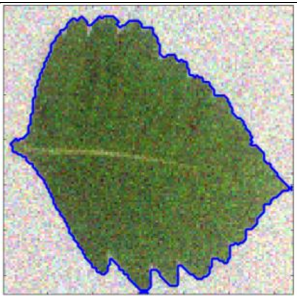 10.1	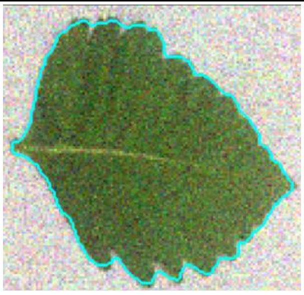 10.2
	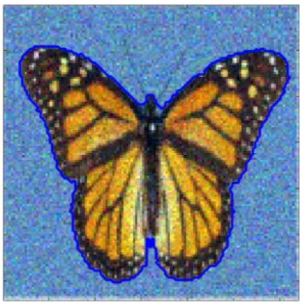 11.1	 11.2
	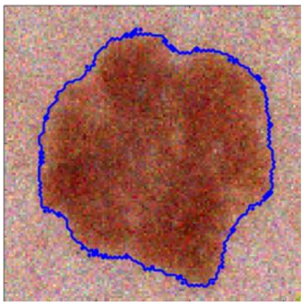 12.1	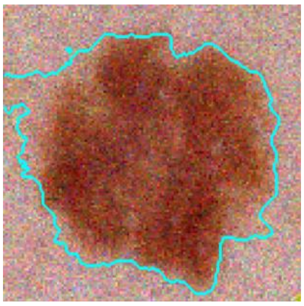 12.2

To provide a comprehensive evaluation, quantitative analysis is conducted using all 80 noisy input images. The performance is measured using JSC, DSC, the accuracy metric, and the error metric. Table 3 summarizes the average performance of the developed GSWNC model (M3) and the work by Azam et al. (2023) (M4) across all input images.

Table 3

The Average Quantitative Result for All Input Images for All Models

Exp/ Model	M3	M4
	Jaccard/Dice/Accuracy/Error/Processing Time (seconds)	
Exp 1 σ^2=0.0001, L=1000	0.8898/ 0.9404/ 0.9451/ 0.0549/ 24.3718	0.8522/ 0.9189/ 0.9286/ 0.0714/ 0.0707
Exp 2 σ^2=0.0009, L=500	0.8900/ 0.9405/ 0.9451/ 0.0549/ 26.1856	0.8550/ 0.9207/ 0.9301/ 0.0699/ 0.0578
Exp 3 σ^2=0.001, L=100	0.8909/ 0.9410/ 0.9456/ 0.0544/ 24.2263	0.8609/ 0.9242/ 0.9318/ 0.0682/ 0.0665
Exp 4 σ^2=0.01, L=50	0.8958/ 0.9439/ 0.9478/ 0.0522/ 24.0204	0.8556/ 0.9211/ 0.9289/ 0.0711/ 0.0588

According to Table 3, image segmentation with a highly severe mixture of AGMG noise, as evaluated in Exp 4, suggests that the GSWNC model (M3) achieves the highest DSC and JSC values compared to other experiments and existing models. The results revealed an average JSC value of 0.8958 for M3, which is 4.7% higher than that of M4. Obviously, the average DSC value is obtained from the same experiment; M3 recorded 0.9439, which is 2.48% higher than M4. Furthermore, Table 3 indicates that M3 leads with an average accuracy of 0.9478 for segmenting images with intensity inhomogeneity distorted by very severe mixed AGMG noise, and M3's average error is naturally the lowest. In conclusion, M4 produced unsatisfactory segmentation outcomes for images affected by intensity inhomogeneity as well as mixed AGMG noise, consistent with Azam et al. (2023), which focused on colorization techniques for image segmentation using CNN models without addressing these challenges. In contrast, the proposed model (M3) is specifically designed to handle both intensity inhomogeneity and noise, demonstrating robust segmentation performance across diverse image types, including natural and medical images.

In terms of computational efficiency, Table 3 demonstrates that M4, a deep learning model, exhibits a significantly shorter testing processing time than M3. For example, in Exp 1, where images were corrupted by low noise, M4 achieved an average processing time of 0.0707 seconds, compared to 24.3718 seconds for M3. This difference is expected, as M3 employs a more complex energy formulation to effectively handle intensity inhomogeneity and mixed AGMG noise. Nevertheless, M4 was burdened by a training period of approximately 240 seconds; in contrast, our proposed variational ACM operates without any training stage, thereby offering immediate computational readiness. Additionally, although computationally more expensive, M3 is independent of data size and demonstrates better segmentation accuracy and consistency across varying image conditions than M4. Therefore, M3 is more suitable for applications that require reliable, high-quality segmentation. In contrast, M4 is more appropriate for time-sensitive applications, but its performance degrades under intensity inhomogeneity and mixed AGMG noise, resulting in less precise and less robust segmentation outcomes.

CONCLUSION

To conclude, our proposed GSWNC model is an effective variational global ACM for segmenting vector-valued intensity inhomogeneity images exposed to a mixture of AGMG noise. This achievement results from adapting dual denoising terms and integrating them with local image information. In addition, these terms can help our model enhance images and recover AGMG noise for segmentation. In particular, the solution of the GSWNC model involves the Calculus of Variations, minimizing the GSWNC model to obtain the Euler-Lagrange (EL) equation, and then applying a finite-difference approach to numerically compute it. This research is also supported by numerical assessments of the models, including several experiments on the segmentation of intensity-inhomogeneous images with low, moderate, severe, and very severe AGMG noise mixtures. As a result, our proposed GSWNC model achieves better image segmentation performance than existing models, as measured by JSC, DSC, and accuracy, while also achieving the lowest error. However, our model produces the second-highest processing time, while the comparative model M2 has the highest due to its complex formulation, whereas M4 exhibits a significantly lower processing time owing to its deep learning-based implementation. In the era of technology, digital images are often affected by a combination of noise, particularly AGMG noise. Therefore, our GSWNC model is a more practical and recommended model in segmenting intensity inhomogeneity in images with mixed AGMG noise. In future studies, we intend to explore other algorithms to reduce computational costs. Additionally, the GSWNC model will be implemented on 3D vector-valued intensity inhomogeneity images corrupted by different noise intensities using a mixture of AGMG noise.

ACKNOWLEDGMENT

The authors thank the Institute for Big Data Analytics and Artificial Intelligence (IBDAAI), Universiti Teknologi MARA, Shah Alam, for its support of this research. The author declares no conflict of interest. All work presented is original, and the research was carried out independently, with no financial or personal interests affecting the results.

REFERENCES

Ali, H., Rada, L., & Badshah, N. (2018). Image segmentation for intensity inhomogeneity in presence of high noise. *IEEE Transactions on Image Processing*, *27*(8), 3729–3738. https://doi.org/10.1109/TIP.2018.2825101

Ali, S. N., & Hasan, T. (2026). Phi-SegNet: Phase-integrated supervision for medical image segmentation. *IEEE Transactions on Medical Imaging*, *61*(11), 1–10. http://arxiv.org/abs/2601.16064

Anter, A. M., & Abualigah, L. (2023). Deep federated machine learning-based optimization methods for liver tumor diagnosis: A review. *Archives of Computational Methods in Engineering*, *30*(5), 3359–3378. https://doi.org/10.1007/s11831-023-09901-4

Ataş, İ. (2023). Performance evaluation of jaccard-dice coefficient on building segmentation from high resolution satellite images. *Balkan Journal of Electrical and Computer Engineering*, *11*(1), 100–106. https://doi.org/10.17694/bajece.1212563

Aubert, G., & Aujol, J.-F. (2008). A variational approach to removing multiplicative noise. *SIAM Journal on Applied Mathematics*, *68*(4), 925–946. https://doi.org/10.1137/060671814

Azam, A. S. B., Jumaat, A. K., & Ibrahim, S. (2023). *Comparison of various colorization techniques for MRI brain tumor segmentation using convolutional neural networks.* 8th International Conference on Recent Advances and Innovations in Engineering: Empowering Computing, Analytics, and Engineering through Digital Innovation, ICRAIE 2023. https://doi.org/10.1109/ICRAIE59459.2023.10468529

Badrinarayanan, V., Handa, A., & Cipolla, R. (2017). SegNet: A deep convolutional encoder-decoder architecture for image segmentation. *IEEE Transactions on Pattern Analysis and Machine Intelligence*, *39*(12), 2481–2495. http://arxiv.org/abs/1505.07293

Badshah, N., Rabbani, H., & Atta, H. (2020). On local active contour model for automatic detection of tumor in MRI and mammogram images. *Biomedical Signal Processing and Control*, *60,* 101993. https://doi.org/10.1016/j.bspc.2020.101993

Badshah, N., Ullah, F., & Matiullah. (2018). On segmentation model for vector valued images and fast iterative solvers. *Advances in Difference Equations*, *2018*(1), 221. https://doi.org/10.1186/s13662-018-1669-9

Bougourzi, F., Dornaika, F., & Hadid, A. (2026). *Decoding matters: Efficient mamba-based decoder with distribution-aware deep supervision for medical image segmentation*. arXiv preprint. http://arxiv.org/abs/2603.12547

Caselles, V. (1995). Geometric models for active contours. *Proceedings of the International Conference on Image Processing*, *3*, 9–12. https://doi.org/10.1109/ICIP.1995.537567

Chan, T. F., & Vese, L. A. (2001). Active contours without edges. *IEEE Transactions on Image Processing*, *10*(2), 266–277. https://doi.org/10.1109/83.902291

Chan, T. F., Yezrielev Sandberg, B., & Vese, L. A. (2000). Active contours without edges for vector-valued images. *Journal of Visual Communication and Image Representation*, *11*(2), 130–141. https://doi.org/10.1006/jvci.1999.0442

Chen, M.-Y., Yang, Y.-H., Ho, C.-J., Wang, S.-H., Liu, S.-M., Chang, E., Yeh, C.-H., & Ouhyoung, M. (2012). Automatic Chinese food identification and quantity estimation. *SIGGRAPH Asia 2012 Technical Briefs*, 1–4. https://doi.org/10.1145/2407746.2407775

Chithra, K., & Santhanam, T. (2018). A novel denoising technique for mixed noise removal from grayscale and color images. *Journal of Theoretical and Applied Information Technology*, *96*(3), 626–642.

Chumchob, N., Chen, K., & Brito-Loeza, C. (2013). A new variational model for removal of combined additive and multiplicative noise and a fast algorithm for its numerical approximation. *International Journal of Computer Mathematics*, *90*(1), 140–161. https://doi.org/10.1080/00207160.2012.709625

Dalavai, L., Purimetla, N. M., Roja, D., Vellela, S. S., Syamsundararao, T., Vuyyuru, L. R., & Kumar, K. K. (2024). *Improving deep learning-based image classification through noise reduction and feature enhancement.* 2024 International Conference on Artificial Intelligence and Quantum Computation-Based Sensor Applications, ICAIQSA 2024 - Proceedings. https://doi.org/10.1109/ICAIQSA64000.2024.10882201

Ding, K., & Weng, G. (2017). *Improved region-scalable fitting model with robust initialization for image segmentation.* 2017 IEEE 2nd International Conference on Signal and Image Processing, 111–115. https://doi.org/10.1109/SIPROCESS.2017.8124516

Ding, K., Xiao, L., & Weng, G. (2017). Active contours driven by region-scalable fitting and optimized Laplacian of Gaussian energy for image segmentation. *Signal Processing*, *134*, 224–233. https://doi.org/10.1016/j.sigpro.2016.12.021

Fang, J., Liu, H., Zhang, L., Liu, J., & Liu, H. (2019). Fuzzy region-based active contours driven by weighting global and local fitting energy. *IEEE Access*, *7*, 184518–184536. https://doi.org/10.1109/ACCESS.2019.2909981

He, C., Wang, Y., & Chen, Q. (2012). Active contours driven by weighted region-scalable fitting energy based on local entropy. *Signal Processing*, *92*(2), 587–600. https://doi.org/10.1016/j.sigpro.2011.09.004

Hossin, M., & Sulaiman, M. N. (2015). A review on evaluation metrics for data classification evaluations. *International Journal of Data Mining & Knowledge Management Process*, *5*(2), 1–11. https://doi.org/10.5121/ijdkp.2015.5201

Isensee, F., Jaeger, P. F., Kohl, S. A. A., Petersen, J., & Maier-Hein, K. H. (2021). nnU-Net: A self-configuring method for deep learning-based biomedical image segmentation. *Nature Methods, 18*(2). https://doi.org/10.1038/s41592-020-01008-z

Kass, M., Witkin, A., & Terzopoulos, D. (1988). Snakes: Active contour models. *International Journal of Computer Vision*, *1*(4), 321–331. https://doi.org/10.1007/BF00133570

Kollem, S., Reddy, K. R. L., & Rao, D. S. (2019). A review of image denoising and segmentation methods based on medical images. *International Journal of Machine Learning and Computing*, *9*(3), 288–295. https://doi.org/10.18178/ijmlc.2019.9.3.800

Lankton, S., & Tannenbaum, A. (2008). Localizing region-based active contours. *IEEE Transactions on Image Processing*, *17*(11), 2029–2039. https://doi.org/10.1109/TIP.2008.2004611

Li, C., & Fan, Q. (2018). A modified variational model for restoring blurred images with additive noise and multiplicative noise. *Circuits, Systems, and Signal Processing*, *37*, 2511–2534. https://doi.org/10.1007/s00034-017-0675-6

Li, C., Kao, C. Y., Gore, J. C., & Ding, Z. (2007). *Implicit active contours driven by local binary fitting energy*. Proceedings of the IEEE Computer Society Conference on Computer Vision and Pattern Recognition, 1–7. https://doi.org/10.1109/CVPR.2007.383014

Li, C., Kao, C. Y., Gore, J. C., & Ding, Z. (2008). Minimization of region-scalable fitting energy for image segmentation. *IEEE Transactions on Image Processing*, *17*(10), 1940–1949. https://doi.org/10.1109/TIP.2008.2002304

Li, C., Xu, C., Gui, C., & Fox, M. D. (2005). *Level set evolution without re-initialization: A new variational formulation.* Proceedings - 2005 IEEE Computer Society Conference on Computer Vision and Pattern Recognition, CVPR 2005, 430–436. https://doi.org/10.1109/CVPR.2005.213

Li, J., Xia, C., & Chen, X. (2018). A benchmark dataset and saliency-guided stacked autoencoders for video-based salient object detection. *IEEE Transactions on Image Processing*, *27*(1), 349–364. https://doi.org/10.1109/TIP.2017.2762594

Litjens, G., Kooi, T., Bejnordi, B. E., Setio, A. A. A., Ciompi, F., Ghafoorian, M., Van Der Laak, J. A., Van Ginneken, B., & Sánchez, C. I. (2017). A survey on deep learning in medical image analysis. *Medical Image Analysis*, *42*, 60–88. https://doi.org/10.1016/j.media.2017.07.005

Liu, C., Ng, M. K. P., & Zeng, T. (2018). Weighted variational model for selective image segmentation with application to medical images. *Pattern Recognition*, *76*, 367–379. https://doi.org/10.1016/j.patcog.2017.11.019

Liu, X., Song, L., Liu, S., & Zhang, Y. (2021). A review of deep-learning-based medical image segmentation methods. *Sustainability*, *13*(3), 1–29. https://doi.org/10.3390/su13031224

Mabood, L., Badshah, N., Ali, H., Zakarya, M., Ahmed, A., Khan, A. A., Rada, L., & Haleem, M. (2022). Multi-scale-average-filter-assisted level set segmentation model with local region restoration achievements. *Scientific Reports*, *12*(1), 15949. https://doi.org/10.1038/s41598-022-19893-z

Malladi, R., Sethian, J. A., & Vemuri, B. C. (1995). Shape modeling with front propagation: A level set approach. *IEEE Transactions on Pattern Analysis and Machine Intelligence*, *17*(2), 158–175. https://doi.org/10.1109/34.368173

Mazlin, M. S., Jumaat, A. K., & Embong, R. (2023). Absorbing markov chain saliency driven active contour model for digital image boundary extraction. *ESTEEM Academic Journal*, *19*, 86–98.

Minaee, S., Boykov, Y., Porikli, F., Plaza, A., Kehtarnavaz, N., & Terzopoulos, D. (2022). Image segmentation using deep learning: A Survey. *IEEE Transactions on Pattern Analysis and Machine Intelligence*, *44*(7). https://doi.org/10.1109/TPAMI.2021.3059968

Noguerol, T. M., Paulano-Godino, F., Martín-Valdivia, M. T., Menias, C. O., & Luna, A. (2019). Strengths, weaknesses, opportunities, and threats analysis of artificial intelligence and machine learning applications in radiology. *Journal of the American College of Radiology*, *16*(9), 1239–1247. https://doi.org/10.1016/j.jacr.2019.05.047

Othman, M., Abdullah, S. L. S., Ahmad, K. A., Abu Bakar, M. N., & Mansor, A. R. (2016). The fusion of edge detection and mathematical morphology algorithm for shape boundary recognition. *Journal of Information and Communication Technology*, *15*(1), 133–144. https://doi.org/10.32890/jict2016.15.1.6

Pandit, S. (2022). *Flower recognition dataset*. Kaggle. https://www.kaggle.com/datasets/shrutipandit707/flowerrecognitiondataset

Pathak, S., & Sejwar, V. (2017). *Optimized noisy image segmentation using genetic algorithm.* Proceedings of the 2017 International Conference on Intelligent Computing and Control Systems, ICICCS 2017, 1311–1316. https://doi.org/10.1109/ICCONS.2017.8250681

Patil, R. V., & Aggarwal, R. (2024). Edge information based seed placement guidance to single seeded region growing algorithm. *International Journal of Intelligent Systems and Applications in Engineering*, *12*(12s), 753–759. https://doi.org/10.17762/ijritcc.v11i9.9760

Ronneberger, O., Fischer, P., & Brox, T. (2015). U-Net: Convolutional networks for biomedical image segmentation. *Lecture Notes in Computer Science (LNIP)*, *9351*, 234–241. https://doi.org/10.1007/978-3-319-24574-4_28

Rudin, L. I., Osher, S., & Fatemi, E. (1992). Nonlinear total variation based noise removal algorithms. *Physica D: Nonlinear Phenomena*, *60*(1–4), 259–268. https://doi.org/10.1016/0167-2789(92)90242-F

Tian, Y., & Xue, Y. (2020). Variation method overview of image segmentation. *Journal of Physics: Conference Series*, *1487*(1), 1–7. https://doi.org/10.1088/1742-6596/1487/1/012012

Tsai, A., Yezzi, A., & Willsky, A. S. (2001). Curve evolution implementation of the Mumford-Shah functional for image segmentation, denoising, interpolation, and magnification. *IEEE Transactions on Image Processing*, *10*(8), 1169–1186. https://doi.org/10.1109/83.935033

Veesam, V. S., & Babu, B. S. (2017). A relative study on the segmentation techniques of image processing. *International Journal of Computer Engineering in Research Trends*, *4*(5), 2349–7084. www.ijcert.org

Vese, L. A., & Chan, T. F. (2002). A multiphase level set framework for image segmentation using the Mumford and Shah model. *International Journal of Computer Vision*, *50*(3), 271–293. https://doi.org/10.1023/A:1020874308076

Wang, F., Huang, H., & Liu, J. (2020). Variational-based mixed noise removal with CNN deep learning regularization. *IEEE Transactions on Image Processing*, *29*, 1246–1258. https://doi.org/10.1109/TIP.2019.2940496

Wang, J., Markert, K., & Everingham, M. (2009). *Learning models for object recognition from natural language descriptions.* British Machine Vision Conference, BMVC 2009 - Proceedings, 1–11. https://doi.org/10.5244/C.23.2

Wu, D., & Yuan, C. (2022). Threshold image segmentation based on improved sparrow search algorithm. *Multimedia Tools and Applications*, *81*(23), 33513–33546. https://doi.org/10.1007/s11042-022-13073-x

Yousaf, N., Amin, J., Butt, W. H., Zafar, A., & Kim, S. (2026). Advanced hybrid transformer CNN framework for improved skin lesion classification and segmentation. *Scientific Reports*. https://doi.org/10.1038/s41598-026-43376-0

Yu, H., He, F., & Pan, Y. (2020). A scalable region-based level set method using adaptive bilateral filter for noisy image segmentation. *Multimedia Tools and Applications*, *79*(9–10), 5743–5765. https://doi.org/10.1007/s11042-019-08493-1

Yuzhenlu. (2022). *PlantSegDatasets*. Kaggle. https://www.kaggle.com/datasets/yuzhenlu/plantseg datasets/data

Zhang, H., Tang, L., & He, C. (2019). A variational level set model for multiscale image segmentation. *Information Sciences*, *493*, 152–175. https://doi.org/10.1016/j.ins.2019.04.04

Zhang, K., Song, H., & Zhang, L. (2010). Active contours driven by local image fitting energy. *Pattern Recognition*, *43*(4), 1199–1206. https://doi.org/10.1016/j.patcog.2009.10.010

Zhao, C., Liu, J., & Zhang, J. (2021). A dual model for restoring images corrupted by mixture of additive and multiplicative noise. *IEEE Access*, *9*, 168869–168888. https://doi.org/10.1109/access.2021. 3137995